Global Biogeochemical Cycles

RESEARCH ARTICLE
10.1029/2017GB005738

Rapid Changes in Anthropogenic Carbon Storage and Ocean Acidification in the Intermediate Layers of the Eurasian Arctic Ocean: 1996–2015

Adam Ulfsbo[1,2], Elizabeth M. Jones[3,4], Núria Casacuberta[5,6], Meri Korhonen[7], Benjamin Rabe[8], Michael Karcher[8,9], and Steven M.A.C. van Heuven[3]

[1]Department of Marine Sciences, University of Gothenburg, Gothenburg, Sweden, [2]Division of Earth and Ocean Sciences, Nicholas School of the Environment, Duke University, Durham, NC, USA, [3]NIOZ Royal Netherlands Institute for Sea Research, Department of Ocean System Sciences, and Utrecht University, Texel, Netherlands, [4]Centre for Energy and Environmental Sciences, University of Groningen, Groningen, Netherlands, [5]Laboratory of Ion Beam Physics, ETH Zurich, Zurich, Switzerland, [6]Institute of Biogeochemistry and Pollutant Dynamics, Environmental Physics, ETH Zurich, Zurich, Switzerland, [7]Finnish Meteorological Institute, Helsinki, Finland, [8]Alfred Wegener Institut Helmholtz Zentrum für Polar- und Meeresforschung, Bremerhaven, Germany, [9]Ocean Atmosphere Systems GmbH, O.A.Sys, Hamburg, Germany

Key Points:
- Rapid decadal accumulation of basin-wide anthropogenic carbon in the Arctic and intermediate layers of the Nansen and Amundsen Basins
- The pH in the upper layers has decreased by 0.0021 ± 0.0004 per year in the Eurasian Basin
- Tracer data and model simulations suggest that C_{ant} accumulation is likely driven by Atlantic source waters, followed by interior transport

Supporting Information:
- Supporting Information S1
- Figure S1
- Figure S2
- Figure S3
- Figure S4
- Figure S5
- Figure S6
- Figure S7
- Table S1
- Table S2

Correspondence to:
A. Ulfsbo,
adam.ulfsbo@marine.gu.se

Citation:
Ulfsbo, A., Jones, E. M., Casacuberta, N., Korhonen, M., Rabe, B., Karcher, M., & van Heuven, S. M. A. C. (2018). Rapid changes in anthropogenic carbon storage and ocean acidification in the intermediate layers of the Eurasian Arctic Ocean: 1996–2015. *Global Biogeochemical Cycles*, *32*, 1254–1275. https://doi.org/10.1029/2017GB005738

Received 4 JUN 2017
Accepted 8 APR 2018
Accepted article online 18 APR 2018
Published online 3 SEP 2018

©2018. The Authors.
This is an open access article under the terms of the Creative Commons Attribution-NonCommercial-NoDerivs License, which permits use and distribution in any medium, provided the original work is properly cited, the use is non-commercial and no modifications or adaptations are made.

Abstract The extended multiple linear regression technique is used to determine changes in anthropogenic carbon in the intermediate layers of the Eurasian Basin based on occupations from four cruises between 1996 and 2015. The results show a significant increase in basin-wide anthropogenic carbon storage in the Nansen Basin (0.44–0.73 ± 0.14 mol C·m^{-2}·year^{-1}) and the Amundsen Basin (0.63–1.04 ± 0.09 mol C·m^{-2}·year^{-1}). Over the last two decades, inferred changes in ocean acidification (0.020–0.055 pH units) and calcium carbonate desaturation (0.05–0.18 units) are pronounced and rapid. These results, together with results from carbonate-dynamic box model simulations and ^{129}I tracer distribution simulations, suggest that the accumulation of anthropogenic carbon in the intermediate layers of the Eurasian Basin are consistent with increasing concentrations of anthropogenic carbon in source waters of Atlantic origin entering the Arctic Ocean followed by interior transport. The dissimilar distributions of anthropogenic carbon in the interior Nansen and Amundsen Basins are likely due to differences in the lateral ventilation of the intermediate layers by the return flows and ramifications of the boundary current along the topographic boundaries in the Eurasian Basin.

1. Introduction

Between 25% and 30% of the total anthropogenic emissions of carbon dioxide (CO_2) to the atmosphere is absorbed by the ocean (Le Quéré et al., 2016). The ocean's capacity to store CO_2 is controlled by biological (soft tissue and calcification), physical (interior export), and chemical (solubility) processes. Although mitigating climate change, the oceanic uptake of anthropogenic CO_2 (C_{ant}) causes significant changes in ocean carbon chemistry and may ultimately lead to cessation or significant decrease in the inorganic storage of anthropogenic CO_2 in the ocean as the seawater buffering capacity decreases (Hagens & Middelburg, 2016; Hauck & Völker, 2015; Revelle, 1983; Sabine et al., 2004). Uptake of anthropogenic CO_2 inevitably leads to decreasing pH, lower concentration of carbonate ions, and lowered saturation state (Ω) for metal carbonates such as aragonite and calcite, that is, ocean acidification.

Ocean acidification in the Arctic is more pronounced than in any other ocean (Bates et al., 2011; Semiletov et al., 2016; Steinacher et al., 2009; Yamamoto et al., 2012). Saturation states of the calcium carbonate polymorphs aragonite and calcite indicate that most of the waters of the deep basins are oversaturated (Jutterström & Anderson, 2005). However, observations have shown that a number of regions in the Arctic Ocean are already undersaturated with respect to aragonite, for example, the Canada Basin with the Chuckchi and Beaufort Seas (Qi et al., 2017; Wynn et al., 2016; Yamamoto-Kawai et al., 2009), the Canadian Arctic Archipelago and MacKenzie shelves (Chierici & Fransson, 2009; Fransson et al., 2013), and the Laptev and East Sibierian Seas (Anderson et al., 2017; Semiletov et al., 2016). This is primarily caused by freshwater dilution from sea ice melt and riverine input, invasion of anthropogenic CO_2 from the atmosphere at an ice-free

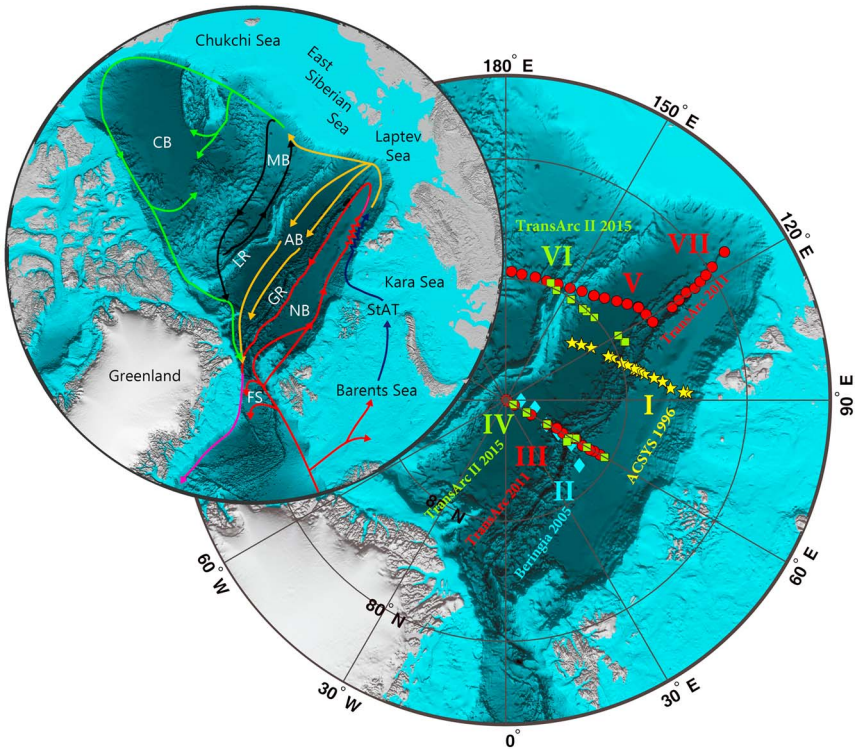

Figure 1. Map of the Arctic Ocean with general circulation patterns in the intermediate layers of the deep basins and exchange with waters of Atlantic origin, adapted after Rudels (2016). Sections in this study are indicated by their roman numerals referred to in the text and Table 1: Arctic Climate System Study 1996 (ACSYS 1996) (I); Beringia 2005 (II); TransArc 2011 (III, V, and VII); and TransArc 2015 (IV and VI). FS = Fram Strait; NB = Nansen Basin; AB = Amundsen Basin; MB = Makarov Basin; CB = Canada Basin; StAT = St. Anna Trough; GR = Gakkel Ridge; and LR = Lomonosov Ridge.

surface ocean, terrestrial organic carbon inputs from rivers, thawing permafrost and coastal erosion, and changes in wind patterns and circulation of source waters.

The Arctic Ocean has a high potential for anthropogenic CO_2 uptake (ΔC_{ant}) and storage (C_{ant}) relative to its size, a feature related to the intense ventilation of subsurface layers and high CO_2 solubility in low-temperature waters. The renewal of intermediate layers is mainly driven by the inflow of ventilated Atlantic water through the Fram Strait and over the Barents Sea and dense water formation by brine release during sea ice production (Rudels et al., 2012). The anthropogenic CO_2 concentration in the Arctic Ocean is nearly twice that of the global mean, and highest C_{ant} concentrations are found at the surface and throughout the intermediate layers, with distinct interbasin differences, whereas the deep waters hold low C_{ant} concentrations (Tanhua et al., 2009). The inorganic carbon inventory of the intermediate layers of the Arctic Ocean has increased during the last two decades, which is attributed to increasing concentrations of anthropogenic carbon in the inflowing Atlantic source waters (Ericson et al., 2014). The Atlantic layer and intermediate water masses flow in a cyclonic pattern along topographic boundaries (Figure 1) before exiting through Fram Strait and beyond to the Atlantic Ocean, thereby linking the Arctic to the global thermohaline circulation (Anderson et al., 1999; Mauritzen, 1996). However, there is relatively little recent information on the inventory and uptake rate of anthropogenic CO_2 in the Arctic Ocean (Tanhua et al., 2013). This is primarily due to the dearth of high-quality seawater CO_2 system data and ancillary biogeochemical variables of sufficient spatial and temporal resolution from which to determine anthropogenic inventory and uptake rates. As a result, the Arctic Ocean has not typically been included in the global estimates of anthropogenic CO_2 (e.g., Khatiwala et al., 2013).

The gradual uptake of anthropogenic CO_2 by the ocean from the atmosphere can, in principle, be quantified as the ensuing gradual rise of dissolved inorganic carbon (DIC) at the surface and eventually within the ocean interior (Brewer, 1978; Chen & Millero, 1979; Postma, 1964). The large and complex natural ocean background provides difficult challenges in order to assess any trends and to distinguish the small anthropogenic component. Several different methods have been developed to estimate the total anthropogenic CO_2 inventory (C_{ant})

Table 1
List of Cruises: Arctic Climate System Study 1996 (ACSYS 1996; ARK-XII; PS41), Beringia 2005 (ODEN05; AOS-2005), and Trans-Arctic Survey of the Arctic Ocean in Transition 2011 (TransArc 2011; ARK-XXVI/3; PS78) and 2015 (TransArc II 2015; ARK-XXIX/3, PS94)

Survey (Section)	EXPOCODE (vessel)	Date	Parameters	Source	Adjustments[a]
ACSYS 1996 (Section I)	06AQ19960712 (R/V *Polarstern*)	12 Jul to 6 Sep 1996	*S*, *T*, O_2, DIC, TA[c], pH, NO_3, PO_4, Si	GLODAPv2[b] (Anderson and Augstein (1996))	
Beringia 2005 (Section II)	77DN20050819 (I/B *Oden*)	19 Aug to 25 Sep 2005	*S*, *T*, O_2, DIC, TA, pH, NO_3, PO_4, Si	GLODAPv2[b] (Anderson, Tanhua, et al., 2011)	TA:+5, pH:+0.01, Si:+0.4
TransArc 2011 (Sections II, V, VII)	06AQ20110806 (R/V *Polarstern*)	6 Aug to 7 Oct 2011	*S*, *T*, O_2[d], DIC, TA, pH, NO_3, PO_4, Si	Schauer et al. (2011) Anderson, Ulfsbo, and Ericson (2011) Kattner and Ludwichowski (2014)	O_2:+2, DIC:-3
TransArc II 2015 (Sections IV, VI)	06AQ20150817 (R/V *Polarstern*)	17 Aug to 15 Oct 2015	*S*, *T*, O_2[e], DIC, TA[f], pH, NO_3, PO_4, Si	Rabe et al. (2016) Jones and Ulfsbo (2017) van Ooijen et al. (2016)	DIC:-2

Note. For the geographic location of the stations for each section and cruise, see Figure 1. The original data source and principal investigator are referred to in parentheses. DIC = dissolved inorganic carbon; TA = total alkalinity; CTD = conductivity-temperature-depth.
[a]Adjustments made in this study. GLODAPv2 adjustments available at https://glodapv2.geomar.de/adjustments/. [b]The ACSYS 1996 and Beringia 2005 data sets were extracted from GLODAPv2 (Key et al., 2015; Olsen et al., 2016). [c]TA calculated from pH and DIC (see section 2). [d]Calibrated CTD oxygen. [e]Noncalibrated CTD oxygen. [f]TA calculated from pH and DIC (see section 2).

since the preindustrial era and to quantify the increase in C_{ant} (ΔC_{ant}). The first category requires knowledge of preindustrial concentrations and transient tracers (e.g., Brewer, 1978; Chen & Millero, 1979; Gruber et al., 1996; Hall et al., 2002; Stöven et al., 2016; Tanhua et al., 2009), whereas the latter relies on linear regression analyses of high-quality repeat hydrographic sections or ocean times series (e.g., Friis et al., 2005; Peng et al., 1998; van Heuven, Hoppema, et al., 2011; Wallace, 1995).

With close to 20 years (1996–2015) of hydrographic and carbonate system data in the Eurasian Basin (Figure 1), we exploit the extended multiple linear regression (eMLR) technique (Friis et al., 2005) in the Atlantic and intermediate layers (~100–1,500 m) of the central Arctic Ocean with respect to changes in anthropogenic CO_2, pH, and aragonite saturation state. The eMLR technique has been widely used to detect decadal changes in anthropogenic carbon throughout the major oceans (e.g., Brown et al., 2010; Carter et al., 2017; Chu et al., 2016; Friis et al., 2005; Sabine et al., 2008; Waters et al., 2011; Woosley et al., 2016) and now in the Eurasian Arctic Ocean.

2. Data Description and Quality

2.1. Data Sets

Data were analyzed from four icebreaker surveys between 1996 and 2015 (Table 1) transecting the Nansen and Amundsen Basins in the Eurasian Arctic Ocean (Figure 1). We refer to the Arctic Climate System Study 1996 (ACSYS 1996) cruise (Figure 1; Section I) as the initial occupation, and the progressively more recent Beringia 2005 (Section II), TransArc 2011 (Sections III, V, and VII), and TransArc II 2015 (Sections IV and VI) cruises are assumed reoccupations. It is important to note that the transects are not true repeat surveys with respect to geographical location and vertical and horizontal sampling resolution. The ACSYS 1996 section spans between 82–86°N and 90–120°E, whereas the main sections from 2005 to 2015 are between 85°N and 90°N along 60°E. Two additional sections from 2011 (Section V) and 2015 (Section VI) with an eastern offset from ACSYS 1996 were included, as well as a third section from 2011 along the Gakkel Ridge toward the Laptev Sea (Section VII). The data from 1996 and 2005 were included in the Arctic Ocean data compilation (Jutterström et al., 2010) within the Carbon Dioxide in the Atlantic Ocean (CARINA) data synthesis project (Key et al., 2010) and the more recent Global Ocean Data Analysis Project version 2 (GLODAPv2), which has been subjected to rigorous quality control as described in Key et al. (2015) and Olsen et al. (2016). Data from 2011 and 2015 have not yet been included in these synthesis products; however, they are available from other sources (Table 1).

2.2. Analytical Methods and Quality

Practical salinity (*S*), temperature (*T*), dissolved oxygen (O_2), nitrate (NO_3), phosphate (PO_4), silicate (Si), pH, total alkalinity (TA), and DIC were used in the present study. Briefly, during the 1996–2011 cruises, DIC was determined using a coulometric titration method based on Johnson et al. (1987) with a modified Single Operator Multiparameter Metabolic Analyzer system (coulometer type UIC 5012), a predecessor to the VINDTA 3C (MARIANDA, Kiel, Germany), which was used to measure both DIC and TA in 2015. During the earlier cruises, TA was determined by open cell potentiometric titration according to Haraldsson et al. (1997). For DIC, the precision was 1–2 μmol/kg for all cruises but TransArc 2011, with a precision of about 4 μmol/kg. The precision in TA was better than 2 μmol/kg for all cruises. The accuracy in DIC and TA was ensured by routine analysis of certified reference material (CRM) obtained from A. G. Dickson of Scripps Institution of Oceanography (La Jolla, CA, USA) during all cruises. Seawater pH was determined spectrophotometrically (Agilent 8453) on the total scale with a precision better than 0.001 pH units. The method is based on the absorption ratio of the sulfonephthalein dye m-cresol purple (Clayton & Byrne, 1993). Purified m-cresol purple (Liu et al., 2011) was obtained from R. H. Byrne of University of South Florida (St. Petersburg, USA) for 2015. Conversion of seawater pH between standard (25°C and surface (0 dbar) pressure) and in situ (temperature and pressure) conditions followed the GLODAPv2 quality control methodology (Olsen et al., 2016; Velo et al., 2010). The total pH scale at in situ temperature and pressure was used throughout this study. During the 1996 and 2005 cruises, oxygen was determined with automated Winkler titration systems, with a relative precision of better than 1%. During the 2011 and 2015 cruises oxygen was acquired from a Sea-Bird Electronics (SBE43) oxygen sensor mounted on the conductivity-temperature-depth (CTD) package, with the data calibrated by Winkler titrations only in 2011. Nutrients were measured by autoanalyzers according to standard procedures (e.g., following the World Ocean Circulation Experiment protocol for the earlier cruises Gordon et al., 1994), with a relative precision better than 2%.

Secondary quality control was applied on Eurasian Basin Deep Water (>2,500 m) by offset analysis using multiple linear regression (MLR) for each parameter (Jutterström et al., 2010). There is little variation in Eurasian Basin Deep Water properties as a result of long residence time (Tanhua et al., 2009) with small impact from biogeochemical processes, such as organic matter remineralization and the temporal variability of calcium carbonate dissolution (Ericson et al., 2014). According to Jutterström et al. (2010), the offset (supporting information Figure S1) should be greater than 4 μmol/kg for DIC, 6 μmol/kg for TA, 2% for nutrients and oxygen, and 0.01 for salinity for an adjustment to be made. Although no true offsets were found, adjustments were performed on the entire data sets according to Table 1, based on the notion of invariable deep water mean values over the considered period of this study (Ericson et al., 2014).

The carbonate system was overdetermined (pH, DIC, and TA) during all cruises. The internal consistency, based on the mean differences between measured and calculated parameters, was better than 2 μmol/kg for TA and DIC and 0.005 for pH (Table S1) and thus of the same order of magnitude as the precision of the measurements. For ACSYS 1996 TA was partially calculated from DIC and pH within the CARINA data product, whereas these were excluded in GLODAPv2. In this study, we use TA calculated from DIC and pH for ACSYS 1996 and TransArc II 2015 using the carbonic acid dissociation constants of Lueker et al. (2000), the bisulfate constant of Dickson (1990), and the boron/salinity ratio of Uppström (1974). All calculations were made using the MATLAB CO2SYS version 1.1 (van Heuven, Pierrot et al., 2011).

3. Methods

3.1. Determining Anthropogenic CO_2 Changes

The eMLR technique presented by Friis et al. (2005), a derivative from the MLR approach (Wallace, 1995), was used to assess the short-term increase of C_{ant} (ΔC_{ant}) on decadal scales. Since its introduction, the eMLR technique has been used extensively throughout the major oceans (Brown et al., 2010; Carter et al., 2017; Chu et al., 2016; Hauck et al., 2010; Olsen et al., 2006; Peng & Wanninkhof, 2010; Quay et al., 2007; Sabine et al., 2008; Wanninkhof et al., 2010; Waters et al., 2011; Woosley et al., 2016; Williams et al., 2015). All MLR techniques are empirical approaches that rely on the robust correlation of changes in DIC with changes in other physical and biogeochemical variables throughout an ocean section and account for seasonal and interannual variability between data sets. This inherently assumes that the natural variability in DIC is linearly related to the physical and biogeochemical input variables, while anthropogenic changes are not. In the eMLR approach, DIC from two different years are fit independently applying a MLR to the same set of multiple physical and biogeochemical predictor variables that explain the DIC content for each year. The change (or difference)

in the resultant MLR regression coefficients between the two data sets (years) is then, usually, used in conjunction with the physical and biogeochemical variables from the most recent occupation to estimate ΔC_{ant}. Assuming that hydrographic properties of the water masses and the underlying natural relationship between the input variables and DIC stay the same, physical and biogeochemical variations thence cancel out (Friis et al., 2005; Hauck et al., 2010). The information about C_{ant} is therefore carried only by the regression coefficients and not by the variables. Equations (1) through (3) illustrate the eMLR approach to estimate ΔC_{ant} (μmol/kg) between two occupations,

$$DIC_1^{MLR} = a_1 + b_1 S_1 + c_1 T_1 + d_1 [NO_3]_1 + e_1 [TA]_1 + f_1 [Si]_1, \quad (1)$$

$$DIC_2^{MLR} = a_2 + b_2 S_2 + c_2 T_2 + d_2 [NO_3]_2 + e_2 [TA]_2 + f_2 [Si]_2, \quad (2)$$

$$\begin{aligned} \Delta C_{ant} =& (a_2 - a_1) + (b_2 - b_1) S_2 + (c_2 - c_1) T_2 + (d_2 - d_1) [NO_3]_2 \\ &+ (e_2 - e_1) [TA]_2 + (f_2 - f_1) [Si]_2, \end{aligned} \quad (3)$$

where S, T, NO_3, TA, and Si were used as predictor variables in this study. The subscript 2 indicates variables and regression coefficients from a more recent occupation (Table 1; 2005–2015), and subscript 1 represents regression coefficients from the reference occupation (1996). Physical and biogeochemical variables can, ideally, be used either from the prior occupation (forward case) or from the more recent occupations (backward case), however, the data set with the highest quality should be used to calculate ΔC_{ant} from equation (1) (Tanhua et al., 2007). Consequently, we use the "backward case" throughout this study deeming the more recent data sets (2005–2015) to be of higher quality and of greater spatial coverage compared to the reference occupation (1996, for "forward case"; see supporting information and Figure S2).

The variables used in the MLRs are not universal, and the best choice of variables varies by geographic location and data quality; thus, they must be determined for each data set. The combination of predictor variables in equations (1)–(3) was determined by an iterative stepwise linear regression approach (MATLAB routine "stepwiselm") of all ACSYS 1996 DIC data. The approach uses a t test to determine which variables are significant and an F test to ensure model robustness. Potential temperature (θ), T, S, O_2, apparent oxygen utilization (AOU), TA, Si, NO_3, and PO_4 were considered in different combinations in addition to the final choice of variables (equations (1)–(3)) as determined from the stepwise regression. There was no significant improvement of the statistical fit using potential temperature instead of temperature. The inclusion of either O_2 or AOU to the variables in equations (1)–(3) resulted in highly scattered results with both depth and in space. Neither nutrient changed the statistical fit considerably; however, NO_3 and Si best supported the notion of invariable deep waters with respect to changes in physical and biogeochemical variables over the considered period of time in this study (Ericson et al., 2014). For the MLRs, a robust regression routine was used (MATLAB routine "robustfit") following Carter et al. (2017). The coefficients for each MLR analysis along with root mean square error and MLR residuals are supplemented (Table S2 and Figure S3). The total uncertainty in the eMLR analysis was estimated to be 5–6 μmol/kg, depending on water mass, and values of ΔC_{ant} (Figure 2) below this range should be considered with caution (Appendix A).

3.2. Determining Ocean Acidification

Decreasing pH as a result of increasing anthropogenic CO_2, that is, ΔpH_{ant}, has previously been estimated from the difference in calculated pH including the change in DIC from ΔC_{ant} under the assumption that total alkalinity does not change significantly in time and space (e.g., Waters et al., 2011; Woosley et al., 2016). In this study, we use another approach by taking the ratio of ΔC_{ant} to the buffer factor β_{DIC} as defined by Egleston et al. (2010). The buffer factor β_{DIC} describes the ocean's capacity to buffer changes in $[H^+]$ due to accumulation of CO_2 from the atmosphere ($(\delta \ln[H^+]/\delta DIC)^{-1}$) and, inherently, assumes constant total alkalinity. Similarly, the ratio of ΔC_{ant} to the buffer factor ω_{DIC} was used to estimate the change in aragonite saturation state. The buffer factor ω_{DIC} describes the ocean's capacity to buffer changes in $[CO_3^{2-}]$ due to accumulation of CO_2 from the atmosphere, that is, $(\delta \ln[CO_3^{2-}]/\delta DIC)^{-1}$, which is the same as $(\delta \ln \Omega_{Ar}/\delta DIC)^{-1}$. The buffer factors were included in a modified CO2SYS version 1.1 and validated against the work of Egleston et al. (2010) and the "buffesm" function in the "seacarb" software package (Lavigne & Gattuso, 2010). The explicit expressions of the buffer factors provide means to compare the degree of buffering in different regions at different times and to gain insight into the buffering mechanisms (Egleston et al., 2010). Reductions greater than 0.01 pH units and 0.02 units for aragonite saturation state should be considered with caution (Appendix A).

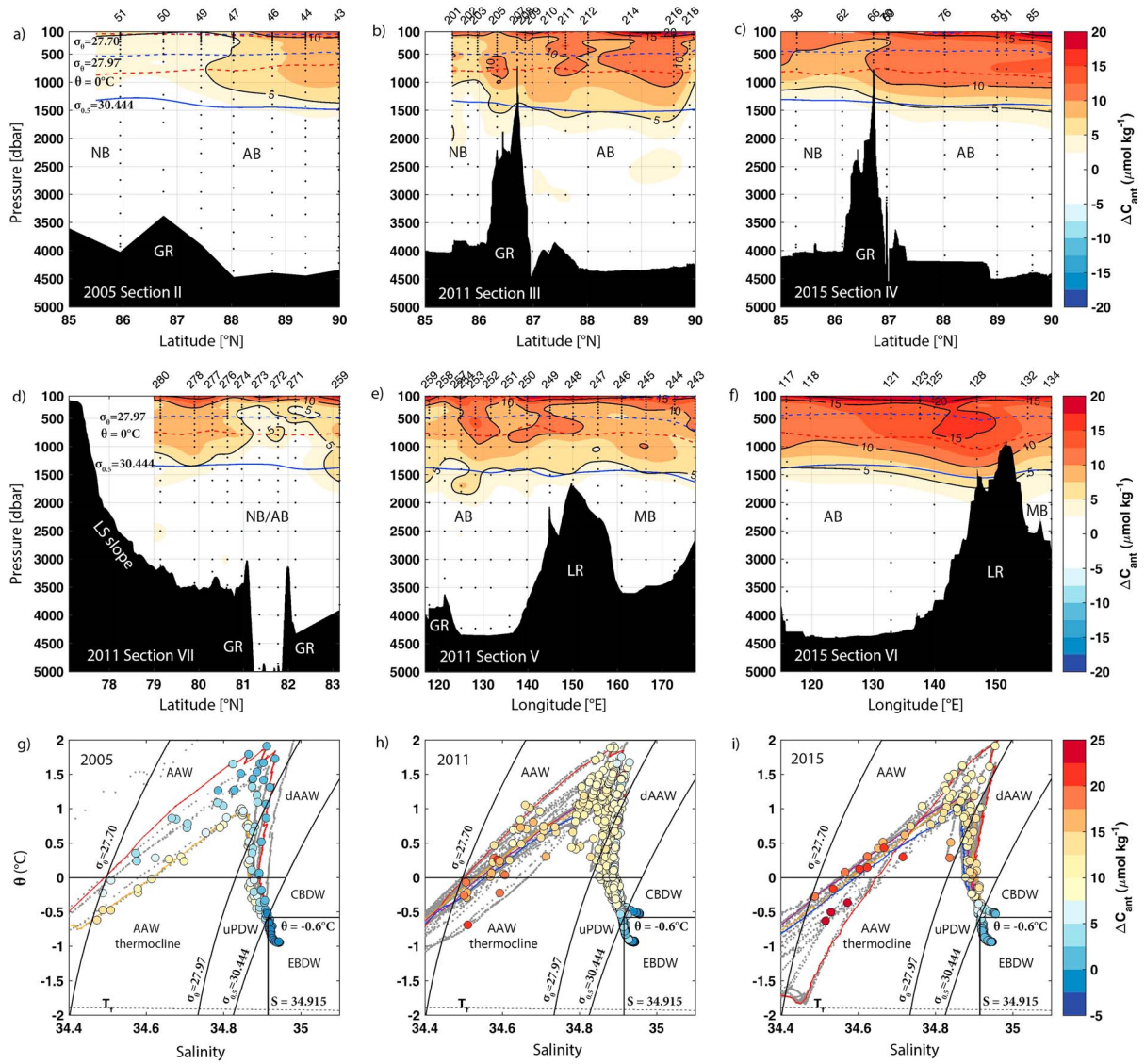

Figure 2. (a–f) Section plots of ΔC_{ant} (μmol/kg) for Beringia 2005 (Figure 1; Section II), TransArc 2011 (Sections III, V, and VII), and TransArc II 2015 (Sections IV and VI) relative to ACSYS 1996 (Section I). CTD stations and sampling depths (black dots) are denoted by their station numbers. Bathymetry is taken from CTD bottom depth in (a) and from the ship's sonar in (b)–(f). Isopycnals (σ_θ = 27.70, σ_θ = 27.97, and $\sigma_{0.5}$ = 30.444) and isothermal (θ = 0°C) used to define each water mass are listed in (a) and shown in all panels. (g–i) Potential temperature-salinity (θ-S) plots with overlaid ΔC_{ant} (μmol/kg) for all stations in 2005, 2011, and 2015. ACSYS 1996 = Arctic Climate System Study 1996; CTD = conductivity-temperature-depth; AAW = Arctic Atlantic Water; dAAW = dense Arctic Atlantic Water; uPDW = upper Polar Deep Water; EBDW = Eurasian Basin Deep Water; CBDW = Canada Basin Deep Water; T_f = seawater freezing temperature, dashed line. AAW thermocline indicates waters defined by 27.70 ≤ σ_θ ≤ 27.97, $\theta \leq 0$, and $S \leq 34.676 + 0.232\theta$. Colored θ-S lines indicate selected CTD stations deemed representative of the Nansen Basin (red), western Amundsen Basin (orange), eastern Amundsen Basin (purple), and the Makarov Basin (blue) for the different years.

3.3. Water Mass Definitions

The water masses of the Eurasian Basin were defined by their S, θ, and density levels (σ_θ, $\sigma_{0.5}$) following Rudels et al. (2012). In this study we refer to Arctic Atlantic Water (AAW; ~100–500 m), dense Arctic Atlantic Water (dAAW; ~500–700 m), upper Polar Deep Water (uPDW; ~700–1,500 m), and deep water (DW; >1,500 m), including both Eurasian Basin Deep Water (EBDW) and Canada Basin Deep Water (CBDW). Surface data (upper ~100 m) was not included in the analysis due to the seasonal changes in the summer and winter mixed layers as a result of brine rejection, physical mixing, and stratification. The depth of the winter mixed layer typically ranges from ~30 to 100 m in the Eurasian Basin (Figure S4). Initial inclusion of surface data provided significant scatter in the eMLR residuals, rendering seemingly poor results. Also, eMLR analysis of data separated into

respective water masses based on isopycnal boundaries (e.g., Wanninkhof et al., 2010; Williams et al., 2015; Woosley et al., 2016) rendered unrealistic results, not consistent with invariable deep water conditions over the time period in this study (Ericson et al., 2014).

4. Results

4.1. Increasing Anthropogenic CO_2

The increase in ΔC_{ant} for all cruises (2005, 2011, and 2015) show similar distribution patterns (Figure 2) in the AAW, dAAW, and uPDW (~100–1,500 m) along the western (Sections II–IV) and eastern (Sections V–VII) sections in the Nansen and Amundsen Basins relative to 1996 (Figure 1 and Section I). For the western sections along 60°N (Figures 1 and 2a– 2c), accumulation of C_{ant} is generally greater at higher latitude with a southward spreading pattern with the Gakkel Ridge as a natural divider between the basins. The same pattern holds for the eastern sections (Figures 1 and 2d–2f) with greater accumulation eastward, toward the Lomonosov Ridge and the Laptev Sea slope. There is no significant change in the deep waters of the central Arctic Ocean, and any apparent deviation from 0 is less than the uncertainty of the analysis (Appendix A).

For all sections, the greatest accumulation is found below the mixed layer in the upper AAW (~100–200 m) in the northern Amundsen Basin. Here we also see local maxima in dAAW and uPDW (~500–1,000 m) in all years. In 2011, there are two additional pronounced features of high ΔC_{ant} values (Figure 2b and Section III): (i) south of the Lomonosov Ridge (89–90°N) and (ii) north and (iii) south of the Gakkel Ridge (87.5–88°N and 86.4°N, respectively). These features of higher ΔC_{ant} at intermediate depth are also seen in the eastern sections (Figures 2e and 2f) in 2011 (Section V) and, partly, in 2015 (Section VI). This suggests that the highest increase in C_{ant} is associated with the propagation of the boundary current and its ramifications north of the Laptev Sea followed by interior transport along the submarine ridges. The absence of the high ΔC_{ant} feature along the Gakkel Ridge at intermediate depth in 2015 (Section VI) compared to 2011 is attributed to the lack of data between 120°E and 140°E during the former cruise. The lowest ΔC_{ant} is mainly found in the Nansen Basin during all cruises, as well as for the section along the Gakkel Ridge (Section VII) in 2011 (Figure 2d), with increasing ΔC_{ant} toward the Laptev Sea slope and the boundary current. There is a similar increase of ΔC_{ant} in the Makarov Basin as in the Amundsen Basin, with higher accumulation in the eastern parts of the basins. For the western sections (Figures 2a–2c), the horizon of significant ΔC_{ant} (>5 μmol/kg) is shoaling from 1,500 to 1,000 m between 90°N and 85°N, following the isopycnal separating the DW and uPDW ($\sigma_{0.5} = 30.444$). For the eastern sections (Figures 2e and 2f), this horizon deepens slightly toward the Lomonosov Ridge. The ΔC_{ant} results for all stations from each year are shown in Figures 2g–2i where selected stations (colored lines) outline the representative θ-S properties of the different water masses in the Nansen, Amundsen, and Makarov Basins for 2005, 2011, and 2015. The warm core of the AAW in the Nansen Basin becomes cooler and fresher crossing the Gakkel Ridge to the Amundsen Basin and even cooler and fresher crossing the Lomonosov Ridge to the Makarov Basin. Similar patterns, albeit less pronounced, are true for the deeper dAAW and uPDW. The greatest increase in ΔC_{ant} in the upper part of the AAW includes the Arctic Ocean thermocline. The anthropogenic changes in AAW, dAAW, and uPDW are more evident in the Amundsen Basin (Figures 2g–2i; orange and purple lines) compared to the Nansen Basin (red line). In 2015, the selected station in the Nansen Basin includes properties of the winter mixed layer with a temperature minimum close to freezing temperatures.

The increase in integrated column inventories ($\Delta C_{ant}/\Delta t$) during the last two decades are given for each water mass and basin in Table 2. Overall, there is a significant increase in basin-wide anthropogenic carbon storage ranging from 0.44 to 0.73±0.14 mol C·m^{-2}·year^{-1} in the Nansen Basin and 0.63 to 1.04±0.09 mol C·m^{-2}·year^{-1} in the Amundsen Basin. Column inventories are estimated by integrating over the depth of the water masses (~100–1,500 m) of significant ΔC_{ant} and dividing by the years between occupations.

4.2. Ocean Acidification and Buffer Capacity

As a result of increasing anthropogenic CO_2, seawater pH and aragonite saturation state decrease. Both ΔpH_{ant} (Figure 3) and $\Delta\Omega Ar_{ant}$ (Figure 4) show similar distribution patterns as ΔC_{ant} (Figure 2), as is expected since they are calculated from ΔC_{ant} (Figure 3) and the explicit buffer factors β_{DIC} and ω_{DIC} (Figure 5), respectively. Both buffer factors show similar (reverse) distribution patterns to ΔC_{ant} (Figure 2): (i) lowest values in the upper AAW (including the thermocline), (ii) low values in both the dAAW and uPDW, and (iii) higher values in the lower part of the AAW and throughout the DW. The lower values in the upper AAW, dAAW, and uPDW are associated with slightly higher DIC/TA mean ratios (~0.943) compared to the AAW and DW (~0.938). As the DIC/TA ratio increases and approaches unity, the buffer factors are near their minimum. The higher ratios

Table 2
Mean Column Inventories, $\Delta C_{ant}/\Delta t$, (mol C·m^{-2}·year^{-1}) Separated by Water Mass and Basin as Annual Rates Calculated Over the Time Period 1996 to 2015

Water mass	Nansen Basin	Amundsen Basin	Eurasian Basin
AAW upper	0.73 ± 0.14	1.04 ± 0.16	0.85 ± 0.17
AAW	0.58 ± 0.13	0.75 ± 0.10	0.65 ± 0.16
dAAW	0.54 ± 0.12	0.72 ± 0.05	0.56 ± 0.15
uPDW	0.44 ± 0.16	0.63 ± 0.09	0.46 ± 0.17
Mean	0.50 ± 0.14	0.69 ± 0.09	0.54 ± 0.16

Note. Inventories were determined by depth integrating significant ΔC_{ant} (>5 μmol/kg). The spread within each water mass and basin is represented by the standard deviation. AAW = Arctic Atlantic Water; dAAW = dense Arctic Atlantic Water; uPDW = upper Polar Deep Water.

in the intermediate layers are attributed to the increasing anthropogenic CO_2 at these depths, signifying that these water masses are particularly sensitive to the increasing anthropogenic CO_2 and, thus, ocean acidification. Over the last two decades (1996–2015), pH decreased by 0.020–0.055 units and the saturation state of aragonite was reduced by 0.05–0.18 units depending on water mass and basin. Annual mean rates of ocean acidification ($\Delta pH_{ant}/\Delta t$ and $\Delta\Omega Ar_{ant}/\Delta t$) for each water mass and basin are given in Table 3. It is worth to note that the two different approaches (Egleston et al., 2010; Woosley et al., 2016) to estimate the anthropogenic change in pH and ΩAr as a result of increasing C_{ant} mentioned in section 3.2 provided similar results (Figure S5).

5. Discussion

During the last two decades, there is an evident increase in the accumulation of anthropogenic CO_2 with consecutive ocean acidification in the intermediate layers of the Eurasian Basin. The change in anthropogenic CO_2 at these intermediate depths is rapid, and the distribution patterns suggest that ramifications of source waters of Atlantic origin have a predominant role in the acidification of the Arctic Ocean interior. As the input of C_{ant} occurs at the atmosphere-ocean interface, we put our results in the context of (i) source waters and ventilation of the intermediate layers (sections 5.1 and 5.2), (ii) the distribution of artificial radionuclides as tracers of Atlantic waters in the Eurasian Arctic Ocean (section 5.3), and (iii) simulations from a carbonate-dynamic box model (section 5.4).

5.1. Intermediate Layers and Source Waters

The intermediate layers of the Arctic Ocean have an Atlantic origin (e.g., Rudels et al., 2012). The only warm water from lower latitudes entering the Eurasian side of the Arctic Ocean is that carried by the Norwegian

Table 3
Mean Rates of Ocean Acidification Expressed as Decrease in pH and ΩAr in Units Per Year (×10^{-4})

	Water mass	Nansen Basin	Amundsen Basin	Eurasian Basin
$\Delta pH_{ant}/\Delta t$	AAW upper	−18 ± 3.7	−26 ± 4.2	−21 ± 4.4
	AAW	−14 ± 3.2	−19 ± 2.6	−16 ± 4.1
	dAAW	−13 ± 3.0	−18 ± 1.3	−14 ± 3.8
	uPDW	−10 ± 3.9	−15 ± 2.3	−11 ± 4.2
	All	−12 ± 3.6	−16 ± 2.2	−13 ± 4.1
$\Delta\Omega Ar_{ant}/\Delta t$	AAW upper	−40 ± 8.8	−60 ± 10.0	−48 ± 11.0
	AAW	−31 ± 7.4	−42 ± 6.1	−36 ± 9.6
	dAAW	−30 ± 6.9	−40 ± 3.1	−32 ± 8.7
	uPDW	−22 ± 8.7	−33 ± 5.5	−23 ± 9.4
	All	−26 ± 8.1	−36 ± 5.3	−28 ± 9.3

Note. The spread within each water mass and basin is represented by the standard deviation. AAW = Arctic Atlantic Water; dAAW = dense Arctic Atlantic Water; uPDW = upper Polar Deep Water.

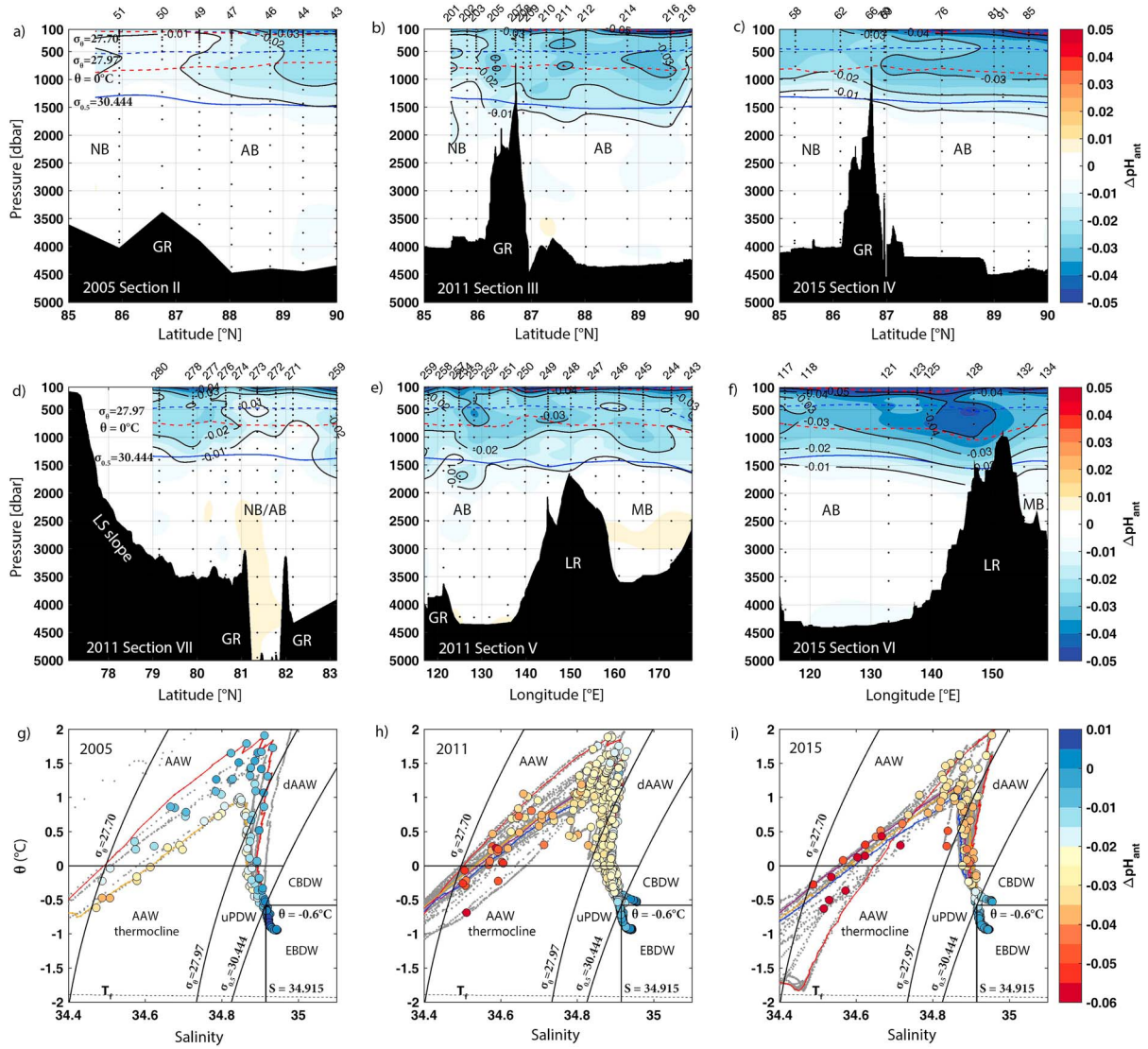

Figure 3. (a–f) Section plots of inferred ΔpH_{ant} for Beringia 2005 (Figure 1; Section II), TransArc 2011 (Sections III, V, and VII), and TransArc II 2015 (Sections IV and VI) relative to ACSYS 1996 (Section I). (g–i) Potential temperature-salinity (θ-S) plots with overlaid ΔpH_{ant} for all stations in 2005, 2011, and 2015. Colored θ-S lines indicate selected CTD stations deemed representative of the Nansen Basin (red), western Amundsen Basin (orange), eastern Amundsen Basin (purple), and the Makarov Basin (blue) for the different years. See Figure 2 for abbreviations.

Atlantic Current, which supplies both the Fram Strait and the Barents Sea inflow branches (Rudels, 2016; Figure 1). The Fram Strait branch is supplied by the extension of the Norwegian Atlantic Current, the West Spitsbergen Current, of which a fraction, the Fram Strait branch water, flows eastward along the Eurasian continental slope forming a boundary current (Pnyushkov et al., 2015; Rudels et al., 2012). The Barents Sea branch is modified by cooling and is freshened by sea ice melt water during summer and brine addition from sea ice production in winter, as well as mixing with the Norwegian Coastal Current (Gascard et al., 2004). Part of the Barents Sea branch enters the Arctic Ocean through St. Anna Trough and then joins the eastward flowing boundary current with the Fram Strait branch. The mean contributions of the two Atlantic branches to the boundary current are of similar magnitude, but (north of the Laptev Sea) a substantial fraction of the Fram Strait branch water is diverted into the interior of the Nansen Basin, whereas the Barents Sea branch is the main supplier of water to the Atlantic layer in the Amundsen Basin (Aksenov et al., 2010; Rudels et al., 2012; Rudels, 2016). The modifications of the Atlantic water through Fram Strait are more modest than those in the shallow Barents Sea, and the modification history of the two branches may also contribute differently to the anthropogenic signals in the Nansen and Amundsen Basins (Figure 2).

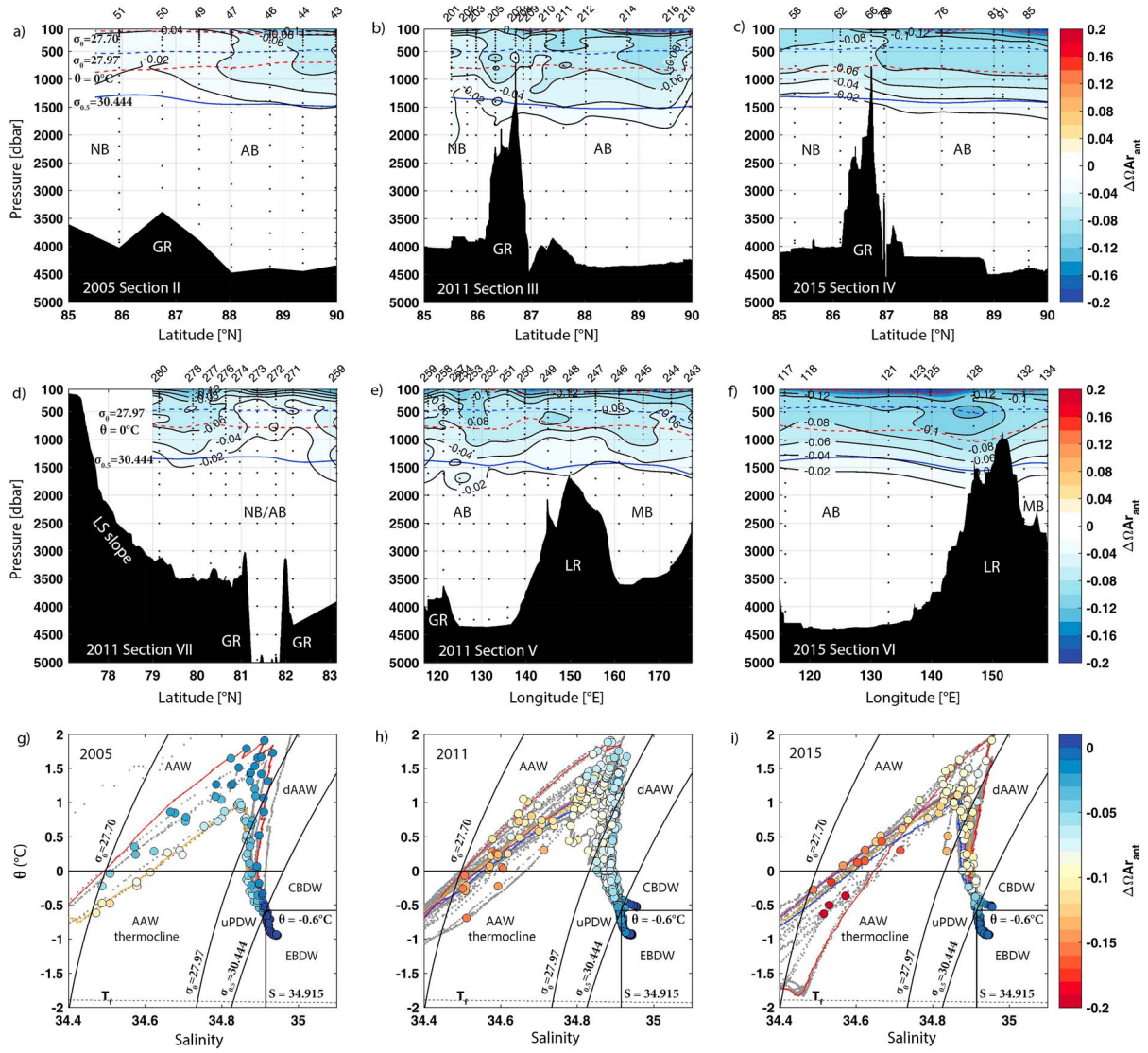

Figure 4. (a–f) Section plots of inferred $\Delta\Omega Ar_{ant}$ for Beringia 2005 (Figure 1; Section II), TransArc 2011 (Sections III, V, and VII), and TransArc II 2015 (Sections IV and VI) relative to ACSYS 1996 (Section I). (g–i) Potential temperature-salinity (θ-S) plots with overlaid $\Delta\Omega Ar_{ant}$ for all stations in 2005, 2011, and 2015. Colored θ-S lines indicate selected CTD stations deemed representative of the Nansen Basin (red), western Amundsen Basin (orange), eastern Amundsen Basin (purple), and the Makarov Basin (blue) for the different years. See Figure 2 for abbreviations.

From analysis of the transient change in DIC in the intermediate layers of the Nansen and Amundsen Basins, Ericson et al. (2014) presented significant trends of increasing DIC in the range of 0.6–0.9 μmol·kg^{-1}·year^{-1} for AAW and dAAW, and 0.4–0.6 μmol·kg^{-1}·year^{-1} for uPDW over the period 1994–2011. The increase in DIC is of similar size or lower compared to previous estimates of increasing $\Delta C_{ant}/\Delta t$ in Atlantic source waters (Ericson et al., 2014), for example, 1.0 ± 0.3 μmol·kg^{-1}·year^{-1} in the Norwegian Atlantic Current over the period 1981–2005 (Skjelvan et al., 2008), 0.57–0.67 μmol·kg^{-1}·year^{-1} in the West Spitsbergen Current over the period 1981–2002/2003 (Olsen et al., 2006), and 0.9 μmol·kg^{-1}·year^{-1} in the core of the Atlantic inflow to the Nordic Seas over the same period. Furthermore, Omar et al. (2003) showed that the surface water partial pressure of CO_2 (pCO_2) increased in the Barents Sea over the period 1967–2001 largely followed the atmospheric record, meaning that the C_{ant} concentration would increase correspondingly. The uniform distribution of the increasing surface pCO_2 suggested that the uptake of atmospheric CO_2 takes place prior to entering the Barents Sea (Omar et al., 2003). The results of Ericson et al. (2014) show the basin-wide mean trend of increasing carbon inventory of the intermediate layers. Because no corresponding change in nutrient concentrations was observed, the increase in DIC was explained by increasing concentrations of anthropogenic CO_2 in Atlantic source waters flowing into the Arctic Ocean (Ericson et al., 2014). Correspondingly, they estimated

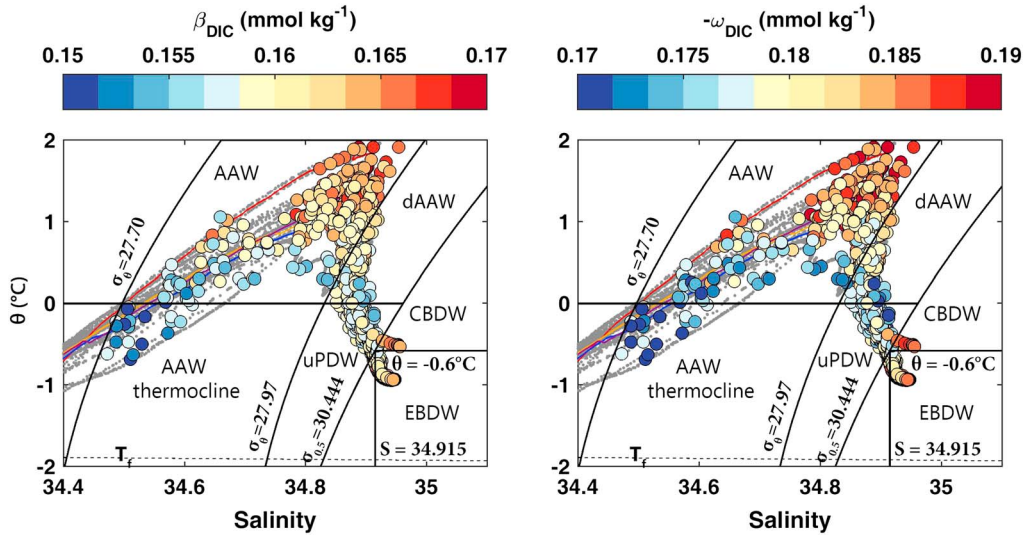

Figure 5. Potential temperature-salinity (θ-S) plots of all data from 2005–2015 with overlaid explicit buffer factors (a) β_{DIC} and (b) the negative of ω_{DIC}. The two buffer factors $((\delta \ln[H^+]/\delta DIC)^{-1}$ and $(\delta \ln \Omega_{Ar}/\delta DIC)^{-1})$ are used together with ΔC_{ant} to estimate ΔpH_{ant} and $\Delta \Omega Ar_{ant}$, respectively. Note the different colorbar scales and unit of concentration. See Figure 2 for abbreviations.

the increase in the integrated carbon column inventory over the Atlantic and intermediate layers of the Nansen and Amundsen Basins to be 0.6 ± 0.1 mol C·m^{-2}·year^{-1} and 0.9 ± 0.1 mol C·m^{-2}·year^{-1}, respectively. This is in good agreement with our estimates of change in integrated column inventories (based on eMLR analysis) for the Nansen Basin (0.44–0.73 ± 0.14 mol C·m^{-2}·year^{-1}) and Amundsen Basin (0.63–1.04 ± 0.09 mol C·m^{-2}·year^{-1}) over the period 1996–2015 (Table 2). Here our results add important information on the spatial distribution of the accumulation of C_{ant} (Figure 2) and we further argue that the accumulation in the interior Nansen and Amundsen Basins is mainly being driven by the increasing concentrations of anthropogenic CO_2 in source waters of Atlantic origin.

The rates of ocean acidification in the intermediate layers of the Amundsen Basin and the upper parts of the AAW in the Nansen Basin (Table 3) are similar to the rates seen in surface waters at long-term ocean carbon time series sites such as Irminger Sea (−0.0026 ± 0.0006 pH units/year), European Station for Time series in the Ocean at the Canary Islands (−0.0018 ± 0.0002 pH units/year), Bermuda Atlantic Time-series Study (−0.0017 ± 0.0001 pH units/year), and Hawaiian Ocean Time-series (−0.0016 ± 0.0001 pH units/year) over the last two to three decades (Bates et al., 2014). Based on ΔC_{ant} from eMLR analysis, Woosley et al. (2016) also found similar rates of ocean acidification (−0.0021 ± 0.0007 pH units/year) in the surface waters (upper 250 m) of the Atlantic Ocean over the period 2003–2014. Our results support the idea of a well-ventilated boundary current at intermediate depth, propagating along the submarine ridges in the Eurasian Arctic Ocean interior.

5.2. Ventilation of Intermediate Layers

At intermediate depths, the Amundsen Basin has been considerably more recently ventilated than the interior Nansen Basin by the return flow of the Barents Sea branch along the Lomonosov Ridge and Gakkel Ridge (Rudels et al., 2012; Tanhua et al., 2009). The return flow of the boundary current in the Nansen Basin, mainly supplied by the Fram Strait branch, follows the southern rim of the Gakkel Ridge. These return flows of ventilated waters are clearly illustrated by the composite section plots of the atmospheric perturbation response (APR) in Figure 6, based on the ΔC_{ant} results from the western and eastern sections from 2011 and 2015 (Figures 2b and 2c). Here, the "atmospheric perturbation response" is defined as the change in seawater pCO_2 relative to the change in atmospheric pCO_2 ($\Delta pCO_2^{sw}{}_{ant}/\Delta pCO_2^{atm}$) over the period 1996–2015. A value near 100% indicates that an interior ocean location is thoroughly ventilated, while low response is indicative of less well-ventilated waters. After a sufficiently long lead time, the APR will approach a constant value reflecting the exposure of an ocean interior location to changes in atmospheric boundary conditions, following the Transient Steady State concept (Gammon et al., 1982; Tanhua et al., 2007). Naturally, lead time would be shortest for those locations that attain the highest APR. The increase in seawater pCO_2 is calculated from the increase in C_{ant} (obtained using eMLR), under the assumption of no change in TA.

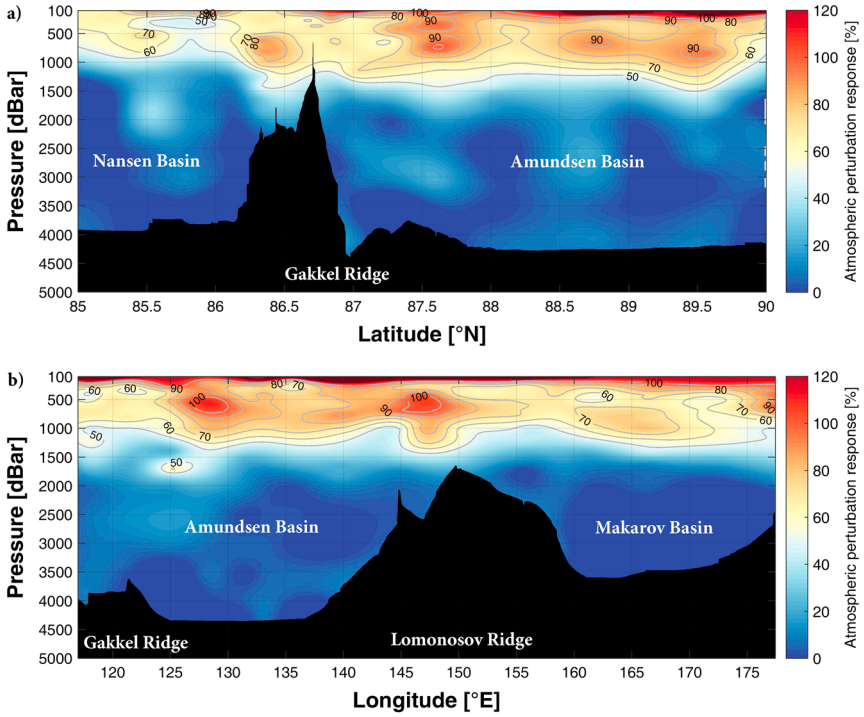

Figure 6. Composite section plots of atmospheric perturbation response for 2011 and 2015 relative to 1996 in the (a) central Eurasian Basin between 85°N and 90°N along 60°E (Sections III and IV; Figure 1) and (b) the eastern Eurasian Basin including the Makarov Basin (Sections V and VI; Figure 1). Values near saturation indicate that the increase in pCO_2 as a result of increasing anthropogenic CO_2 increases at a rate similar to the rate of the increasing atmospheric pCO_2; that is, waters are more recently ventilated with respect to contact with atmosphere and uptake of anthropogenic CO_2 by the ocean.

The rate of increasing atmospheric pCO_2 (~ 2 µatm/year) is derived from Arctic zonal mean xCO_2^{atm} data retrieved from the NOAA Greenhouse Gas Marine Boundary Layer Reference data product (Conway et al., 1994, http://www.esrl.noaa.gov/gmd/ccgg/mbl/). Considering the residence times of the intermediate layers and the time variability in the source waters (Ericson et al., 2014; Tanhua et al., 2009; Smith et al., 2011), this does not necessarily provide the accurate picture of the ventilation. However, the rate of increasing atmospheric pCO_2 has been fairly constant over the last few decades and it highlights the notion of a more recently ventilated boundary current with respect to atmospheric CO_2, supplying the intermediate layers of the Nansen and Amundsen Basins.

5.3. Tracers of Atlantic Water

Measurements of transient tracers such as chlorofluorocarbons (CFCs) and sulfur hexafluoride (SF_6) have been used to estimate the ventilation and C_{ant} storage in, for example, the Arctic Ocean (Tanhua et al., 2009) and Fram Strait (Stöven et al., 2016). The scarcity of transient tracer data in the Arctic Ocean, however, makes it difficult to expand on such an analysis for the time being with respect to C_{ant}. The discharge of anthropogenic radionuclides from nuclear fuel reprocessing facilities into the North Sea allowed the use of radioactive isotopes as tracers of Atlantic waters into the Arctic Ocean (Kershaw & Baxter, 1995). Among these radionuclides, ^{129}I is of special interest for this purpose, as the main source has been the European reprocessing plants of Sellafield (UK) and La Hague (France), with very little input of weapon tests (He et al., 2013). This means that input comes mostly from a single point source of Atlantic origin. ^{129}I released into European coastal waters from nuclear fuel reprocessing plants flow conservatively northward through the Nordic Seas and label the Atlantic water entering the Arctic Ocean (Aldahan et al., 2007; Karcher et al., 2012).

Measurements of the artificial radionuclide ^{129}I from 2011–2012 (Casacuberta et al., 2016) and 2015 (Casacuberta et al., 2018) are compared to our estimates of ΔC_{ant} in the Nansen and Amundsen Basins (Figure 7). A similar distribution pattern of higher ΔC_{ant} and ^{129}I is found in the AAW, dAAW, and uPDW. Values close to 0 for both parameters are found in the deep waters with no significant change between years, corroborating negligible anthropogenic signals to deep and bottom waters. Mean concentrations separated

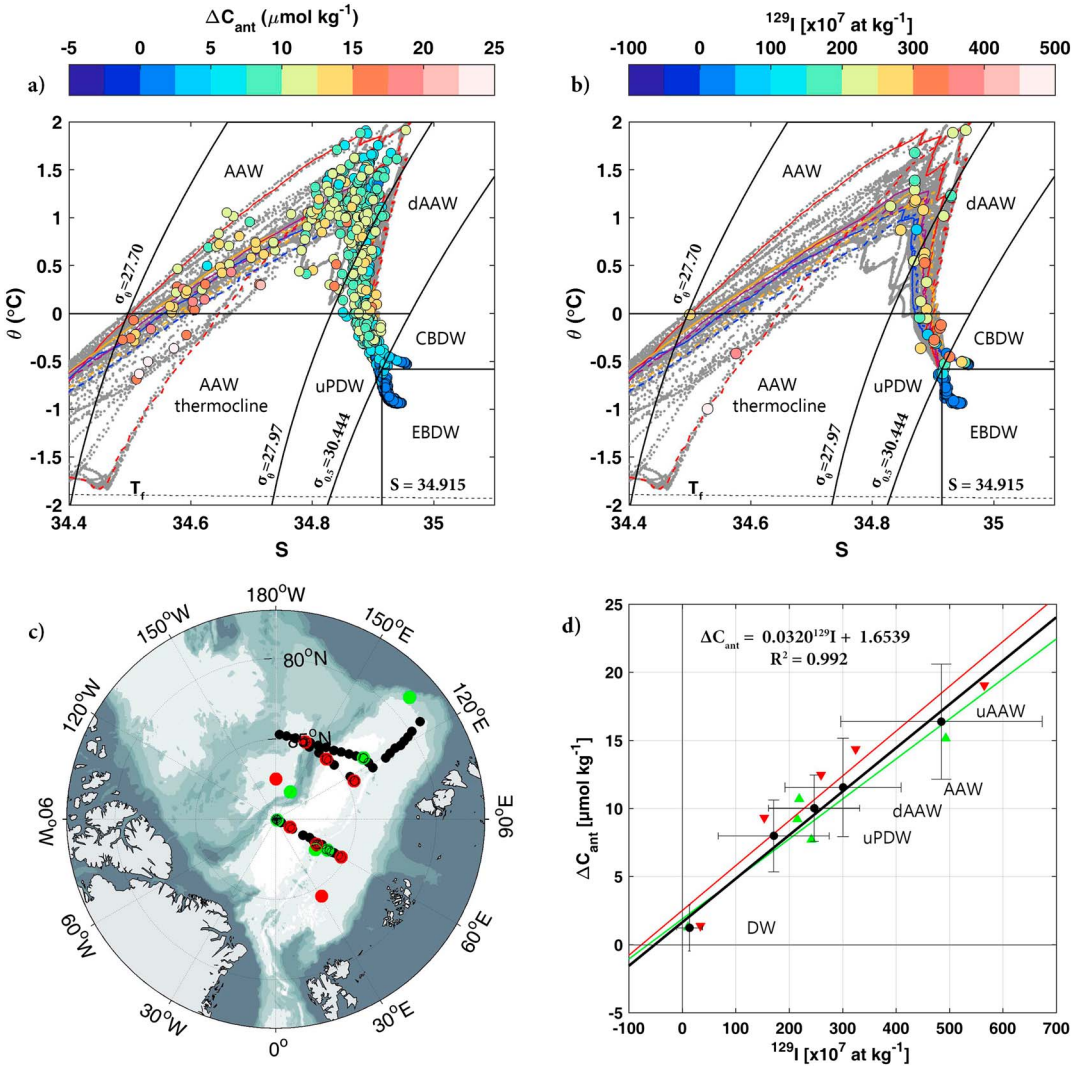

Figure 7. Potential temperature-salinity plots for 2011–2015 with overlaid (a) ΔC_{ant} (μmol/kg) and (b) ^{129}I ($\times 10^7$ at kg^{-1}). (c) Map with station locations of the ΔC_{ant} (2011–2015, black) and ^{129}I (2011–2012, green; 2015, red). (d) Relationship (model type II regression geometric mean) between mean concentrations of ΔC_{ant} and ^{129}I separated by water mass for 2011–2015 (black). The error bars correspond to standard deviations of the data in each water mass. Also shown are the individual mean data for respective water mass from 2011 to 2012 (green; $\Delta C_{ant} = 0.0294 \times {}^{129}I + 1.8904$, $R^2 = 0.991$) and 2015 (red; $\Delta C_{ant} = 0.0329 \times {}^{129}I + 2.5186$, $R^2 = 0.995$).

by water mass (Figure 7d) show a high degree of linear correlation (model type II regression geometric mean). Concentrations of ^{129}I do not necessarily scale perfectly to ΔC_{ant}. They do, however, together with the high degree of linear correlation, support a common anthropogenic signature and distribution pattern of the inflowing Atlantic water. It is worth to emphasize that, while the input of C_{ant} occurs at the atmosphere-ocean interface as a result of increasing atmospheric CO_2 (linear to exponential depending on time scale), ^{129}I originates from point sources in the North Sea with a time dependency input function of ^{129}I (Smith et al., 2011). Karcher et al. (2012) assessed changes in Arctic Ocean circulation using ^{129}I measurements and model simulations of tracer ^{129}I transport through the Arctic Ocean during the period 1970–2010. In this study, we present updated model simulations by Karcher et al. (2012) extended to the years 2011 and 2015 (Figure 8) at representative depths of the AAW (300 m), dAAW (600 m), and uPDW (1,000 m) for comparison. The general distribution patterns of simulated ^{129}I agree well with our estimates of ΔC_{ant}.

The intrusion of Atlantic water into the AAW and dAAW is clearly indicated by elevated ^{129}I concentrations in the Fram Strait and Barents Sea branches along the boundary current. While the boundary current around the continental margins and ridges is relatively confined and energetic, the basin interior is more quiescent.

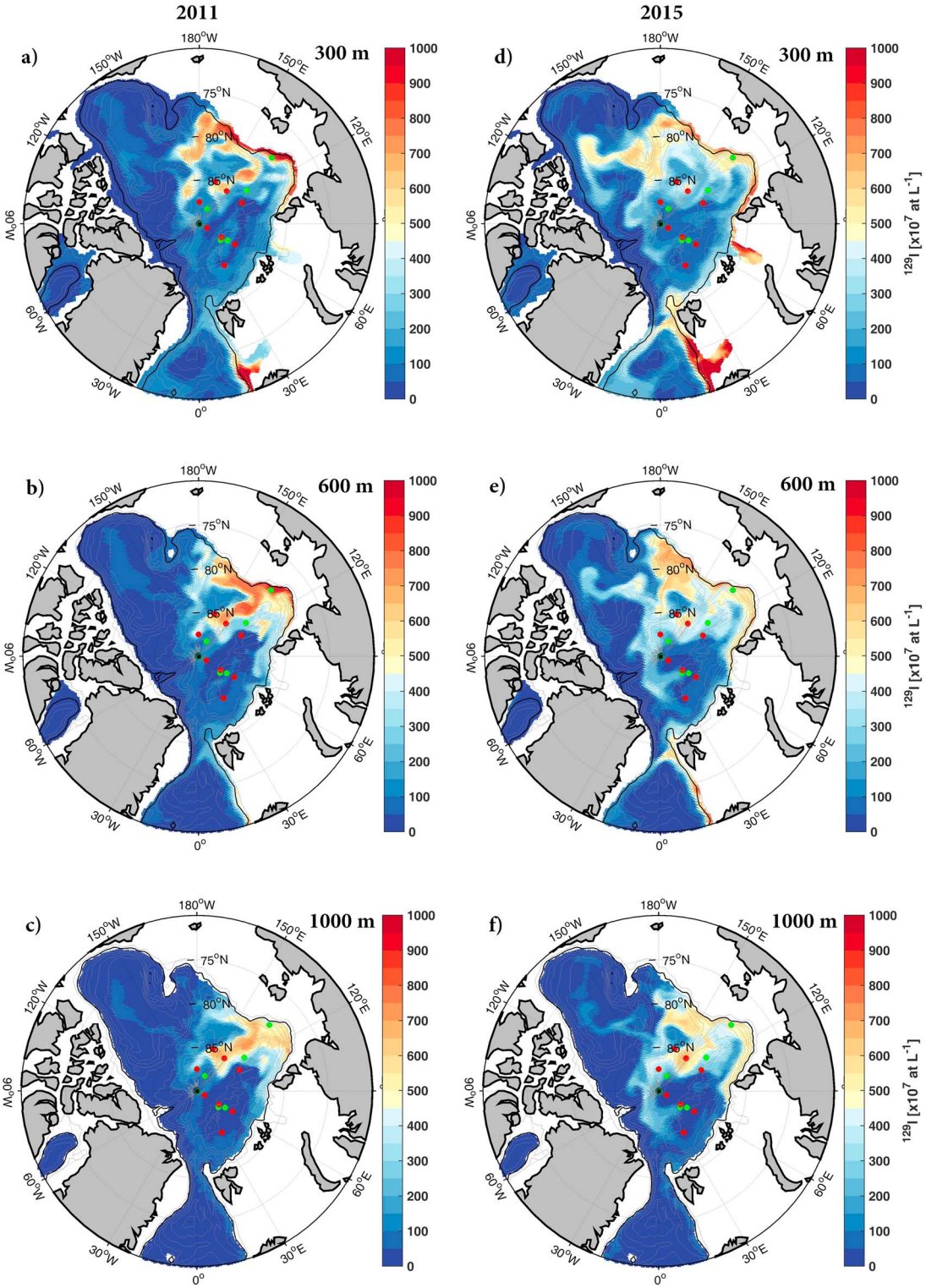

Figure 8. Simulated ^{129}I distributions ($\times 10^7$ at L^{-1}) at (a, d) 300, (b, e) 600, and (c, f) 1,000 m for 2011 and 2015. Model results are updated simulations from Karcher et al. (2012) extended to 2011 and 2015. Markers indicate the station locations of ^{129}I from 2011–2012 (green) and 2015 (red) in Figure 7c, and the black contour line indicates the 1,000 m isobath.

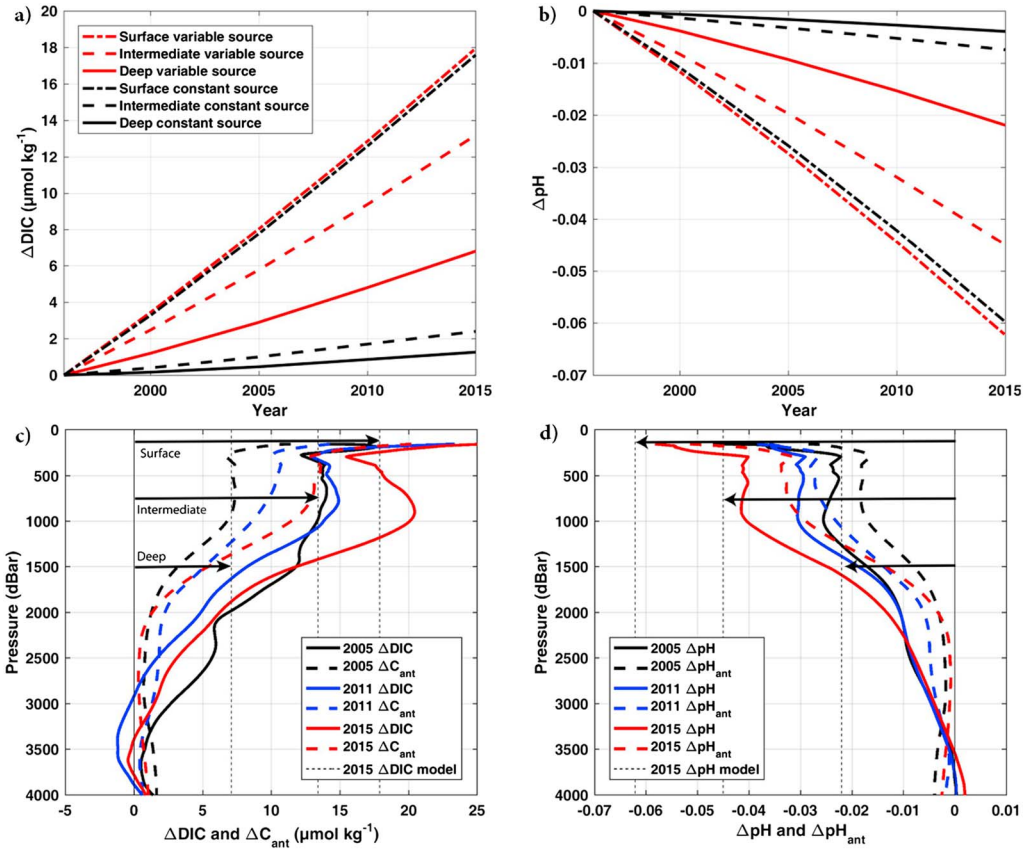

Figure 9. Differences in (a) DIC and (b) pH in the surface, intermediate, and deep water boxes between 1996 and 2015 in the Eurasian Basin from the box model of Luo et al. (2016). The model's DIC and carbonate alkalinity of the inflowing Atlantic and Pacific waters (i) do not change with time (constant source; black lines) and (ii) are allowed to change with time (variable source; red lines), see text for details. Mean profiles of changes in (c) DIC and C_{ant} and, correspondingly, (d) pH and pH_{ant} between 2005 and 2015 relative to 1996. The changes are in relation to the modeled ΔDIC and ΔpH (constant dotted lines) in (a) and (b) for the same period in the surface (0–200 m), intermediate (200–700 m), and deep (>700 m) layers of the Eurasian Basin as indicated by the arrows at representative depths of the layers in the box model.

Hence, any eddy generated in the basin or the dynamic boundary currents (e.g., Karcher et al., 2012; Pnyushkov et al., 2015) would have high impact on inner basin water mass properties. For the uPDW, the contribution of the Fram Strait branch to the boundary current is less evident with respect to ^{129}I, whereas there is a clear intrusion of the Barents Sea Branch via St. Anna Trough. At all depths, bifurcation of the boundary current takes place north of the Laptev Sea, where one part flows along the Lomonosov Ridge toward Greenland, while the other continues into the Makarov and Canada Basins. Along the Lomonosov Ridge, there is a tendency of higher ^{129}I in the dAAW compared to AAW and uPDW. Our results show a similar distribution of higher ΔC_{ant} in these layers, when excluding the upper AAW (100–200 m).

In Karcher et al. (2012), the simulation of ^{129}I circulation in the Arctic indicated that after 2004 the continuation of the boundary current from the Eurasian Basin into the Amerasian Basin via the Makarov Basin had ceased. We find that in the years up to 2015 this situation holds and the Atlantic water spreads the ^{129}I signal along the Lomonosov Ridge and along the Alpha and Mendeleev Ridges. The basic situation is similar for both 2011 and 2015. However, in 2015 we see a strong branch of ^{129}I entering the Amerasian Basin from the north (Figures 8d and 8e). Concentrations in the region between the North Pole and Greenland are higher in 2015, while concentrations in the eastern Eurasian Basin were higher in 2011. Although promising correlations to anthropogenic CO_2 have been found, more detailed studies are warranted on artificial radionuclides as prospective tracers for future applications in deriving changes and distributions of anthropogenic CO_2 in the Arctic Ocean.

5.4. Box Model Simulations

Based on simulations from a carbonate-dynamic box model, Luo et al. (2016) argued for the rapid, near simultaneous acidification of both surface and deeper waters, where deeper waters will be influenced strongly by intrusion of middepth, preacidified, Atlantic water. In this study, we use their default model setup (Boudreau, Middelburg, Hofmann, & Meysman, 2010; Luo et al., 2016) and compare our results to the model simulations of changes in DIC (ΔDIC) and pH (ΔpH) in the surface (0–200 m), intermediate (200–700 m), and deep layers (>700 m) of the Eurasian Basin between 1996 and 2015 (Figures 9a and 9b). In the model, the Arctic atmospheric pCO_2 follows a prescribed CO_2 emission scenario (Boudreau, Middelburg, Hofmann, & Meysman, 2010). The two model runs in Figure 9 illustrate when the DIC and carbonate alkalinity of the inflowing Atlantic and Pacific waters (i) do not change with time (constant source) and, more realistically, (ii) are allowed to change with time (variable source), dictated by the evolving atmospheric CO_2 (Luo et al., 2016). The model applies time-varying DIC and carbonate alkalinity of the Pacific surface and high-latitude Atlantic waters that enter the Arctic obtained from the output of a previously published global carbon system model (Boudreau, Middelburg, Hofmann, & Meysman, 2010; Boudreau, Middelburg, & Meysman, 2010). The variable source run shows a clear increase in DIC and reduction in pH in the intermediate and deep layers compared to the constant condition when DIC and carbonate alkalinity of the inflowing waters do not change with time (see Luo et al., 2016 for details on model setup).

Model results of ΔDIC and ΔpH for 2015 in the Eurasian Basin using the variable source run are compared to mean profiles of measured ΔDIC and ΔpH (2005–2015 relative to 1996) and corresponding mean profiles of ΔC_{ant} and ΔpH_{ant} between 85°N and 90°N along 60°E (Figures 9c and 9d). The constant lines and arrows indicate the change in the parameters given by the model: surface layer (17.9 μmol/kg; −0.062 pH units), intermediate layer (13.4 μmol/kg; -0.045 pH units), and deep layer (7.1 μmol/kg; -0.022 pH units). The ΔC_{ant} and ΔpH_{ant} are consistently lower than ΔDIC and ΔpH, except at deeper depths (~2,500–4,000 m) where no significant anthropogenic change is observed. The modeled increase in ΔDIC of the deep layer agrees well with the observed ΔC_{ant} at ~1,500 m. This may be explained by the fact that the deep layer of the model ranges from 700–4,750 m, hence including large parts of the uPDW (~700–1,500 m) where we find significant accumulation of C_{ant}. Observed ΔC_{ant} in the intermediate layers agree well with the model's intermediate box and the increase in surface box is superceded by ΔC_{ant} in the upper AAW. While there is good agreement between model ΔDIC and ΔC_{ant}, observed ΔpH is more representative of the model results compared to ΔpH_{ant}

The general agreement between observed and modeled changes supports the notion that the increasing C_{ant} in the intermediate layers of the Eurasian Basin is mainly being driven by the increasing anthropogenic CO_2 of the inflowing Atlantic water. Considering analytical uncertainties of ±2–4 μmol/kg in DIC, at least ±0.01 pH units, and uncertainties in the eMLR of 5–6 μmol/kg (~0.01 pH units), both measured ΔDIC and derived ΔC_{ant} are comparable to the model results of the intermediate and deep layers.

Luo et al. (2016) projected surface waters to become undersaturated with respect to aragonite by 2105 and could remain so for ~600 years. In deep waters, the aragonite saturation horizon is projected to rise, reaching the base of the surface mixed layer by 2140. Assuming constant rates of aragonite desaturation (Table 3) and constant ambient conditions with respect to physical and biogeochemical processes, we find similar results of the shoaling of aragonite horizons in the Amundsen Basin (Figure 10) as Luo et al. (2016) suggested for the Eurasian Basin.

Observation-based saturation states of aragonite and calcite indicate that most of the waters of the Eurasian Basin are oversaturated (Figure 10a). However, the Arctic Ocean also demonstrates multibathyal undersaturation with more than one aragonite saturation horizon, a feature found throughout much of the Canada Basin (Jutterström & Anderson, 2005). The western Arctic Ocean has been found to have up to three distinct aragonite undersaturation zones (Wynn et al., 2016): (i) a surface zone (~0–30 m) consistent with carbonate ion dilution by sea ice melt and invasion of anthropogenic CO_2 from the atmosphere, (ii) an Arctic halocline zone (~90–220 m) consistent with remineralization of organic matter on shallow continental shelves bordering the Canada Basin and the input of nutrients and CO_2 entrained by currents of Pacific origin, and (iii) a deep zone (>2,000 m) maintained by relatively low temperatures and stable chemical composition. Recently, Qi et al. (2017) showed that the halocline zone in the western Arctic Ocean had deepened (~150 m) and expanded northward (~ 5°) between the 1990s and 2010. This expansion of aragonite undersaturation was mainly attributed to increased Pacific Winter Water transport, displacing Atlantic Water as a result of an anomalous

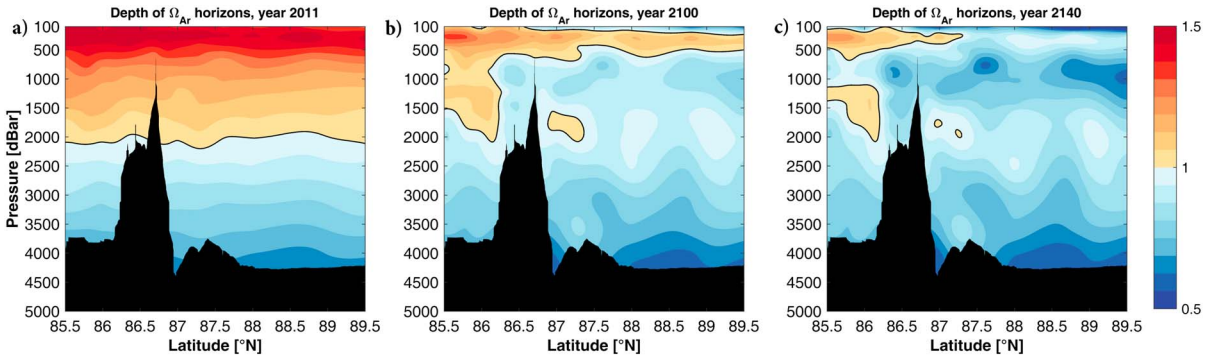

Figure 10. Shoaling of ΩAr horizons in the central Eurasian Basin (along 60°E) over the period 2011–2140 assuming constant rates of C_{ant} accumulation (Table 2) and ambient conditions. (a) Year 2011. (b) Year 2100. (c) Year 2140.

circulation pattern and sea ice retreat. Pacific Water is fresher than the Atlantic Water and it has lower TA and much higher DIC, where biologically driven DIC enrichment and acidification over the shelves add to the latter (Qi et al., 2017). In the Eurasian Basin, which is mainly of Atlantic origin, the surface and halocline zones of aragonite undersaturation are less common features (Jutterström & Anderson, 2005). In this study, surface (0–60 m) aragonite undersaturation and near saturation levels (Figure S6) were only found in 2015 along the eastern Section VI crossing the Lomonosov Ridge (Stations 125–132, Figure 2f), which is attributed to low-salinity river runoff, and/or sea ice melt.

The eastern Eurasian Basin is currently experiencing a shoaling of the Atlantic layer, a weakening in the stratification, and a northward withdrawal of the summer sea ice extent, with increased vertical mixing and winter ventilation as a result (Polyakov et al., 2017). This "atlantification" of the Eurasian Basin and the overall Arctic amplification (e.g., Serreze & Barry, 2011) are expected to become stronger in coming decades and will likely have large impacts on the rate and distribution of ocean acidification in the surface and Atlantic layers of the Eurasian Arctic Ocean.

6. Summary and Conclusions

There is an evident accumulation of anthropogenic CO_2 in the subsurface and intermediate layers of the Eurasian Basin during the last two decades (1996–2015) and inferred changes in ocean acidification and aragonite desaturation are rapid. The increase in anthropogenic CO_2 in the intermediate depths is very likely being driven by the increasing anthropogenic CO_2 of the inflowing Atlantic water. This is supported by finding (i) similar rates of increasing anthropogenic CO_2 at intermediate depths in the interior of the Arctic Ocean as previously reported for Atlantic source waters, (ii) overall agreement between the estimated increase in anthropogenic CO_2 and results from a simple box model driven by increasing atmospheric CO_2 and inflow of Atlantic water, and (iii) strong, positive linear correlation between the distribution of increasing anthropogenic CO_2 and distributions of both observed and modeled anthropogenic ^{129}I, originating from European reprocessing nuclear plants, labeling the Atlantic waters flowing into the Arctic Ocean.

The largest increase in column inventories is found in the Amundsen Basin (0.63–1.04 ± 0.09 mol $C \cdot m^{-2} \cdot year^{-1}$) where the intermediate waters are strongly influenced by intrusion and propagation of recently ventilated water of Atlantic origin, mainly via the Barents Sea Branch. Smaller changes are found in the interior of the Nansen Basin (0.44–0.73 ± 0.14 mol $C \cdot m^{-2} \cdot year^{-1}$), possibly as a result of older recirculating water with input from the Fram Strait branch.

As a result of the increasing accumulation of anthropogenic CO_2, pH is reduced by 0.020–0.055 units during the last two decades. Consequently, this lowers the aragonite saturation state by 0.05–0.18. Assuming constant rates and conditions, it will take less than 100 years for the subsurface and intermediate waters of the Amundsen Basin to become undersaturated with respect to aragonite. The saturation state of aragonite is impacted by several processes, for example, remineralization of organic matter, dilution by sea ice melt, and invasion of anthropogenic CO_2. The combined effect of natural and anthropogenic processes needs to be considered in future assessments of the development of basin-wide aragonite desaturation.

Observation-based studies tend to be biased toward either the Amerasian or Eurasian Arctic Ocean, as is this study. Repeat surveys in the rapidly changing Arctic Ocean have historically been rare and warrant the need for international synoptic efforts, such as the Global Ocean Ship-Based Hydrographic Investigations Program (GO-SHIP) and the GEOTRACES program.

Appendix A: Caveats and Uncertainties

One advantage of the eMLR approach (Friis et al., 2005) compared to the original MLR approach (Wallace, 1995) is that the standard deviation of the eMLR must be lower than the standard deviation of the MLRs because measurement errors go into the prediction twice and partly cancel out when subtracting the regression coefficients from each other (Friis et al., 2005). However, there is still no mechanistic understanding of how errors propagate in an eMLR analysis (Friis et al., 2005; Hauck et al., 2010; Tanhua et al., 2007). Following Hauck et al. (2010), we performed Monte Carlo simulations by randomly disturbing all data sets with a noise on the order of twice the measurement precision: $\delta S = 0.004$, $\delta T = 0.002$°C, $\delta NO_3 = 0.5$μmol/kg, $\delta Si = 0.5$μmol/kg, $\delta TA = 4$μmol/kg, and $\delta DIC = 4$μmol/kg. We used these perturbed data sets to calculate perturbed $\Delta C_{ant}^{1996:2015}$ ($\Delta C_{ant\text{-}error}^{1996:2015}$) 10,000 times and measure precision of our eMLR-based ΔC_{ant} estimates as the standard deviation of all $\Delta C_{ant\text{-}error}^{1996:2015}$ values and accuracy as the difference between the mean $\Delta C_{ant\text{-}error}^{1996:2015}$ and unperturbed $\Delta C_{ant}^{1996:2015}$. The total mean errors for the water masses AAW, dAAW, uPDW, and DW are 4.0 ± 1.1, 4.1 ± 0.8, 4.1 ± 1.0, and 3.0 ± 0.7 μmol/kg, respectively (Figure S7). The total uncertainty (mean error + 2SD) is estimated to be in the range of 5 μmol/kg for the deep waters and 6 μmol/kg for the intermediate layers. Values of ΔC_{ant} below 5–6 μmol/kg (Figure 2), depending on water mass, should be considered with caution. It should also be noted that converting pH from standard temperature (15°C [1996–2011] or 25°C [2015]) and pressure (0 dbar) to in situ temperature and pressure involves using thermodynamic relationships and either TA or DIC. Hence, the results of these calculations are dependent on the choice of dissociation constants used (Woosley et al., 2017) and are associated with uncertainties of the measurements, the strong temperature dependency of seawater pH, and the dissociation constants. Temperatures in the Arctic Ocean are often near or below the valid ranges of most sets of dissociation constants. Furthermore, the pressure dependency of pH is not well constrained (Woosley et al., 2016) and there were no standards or CRM available for seawater pH over the period 1996–2015. It is therefore difficult to determine the accuracy and total uncertainty of the pH measurements. The variables of the marine carbonate system from the different cruises are internally consistent to a high degree, and we assume that the accuracy in pH is better than ±0.01 pH units. For the inferred changes in ocean acidification we apply the total uncertainty from the Monte Carlo perturbation simulations to the calculations of ΔpH_{ant} and $\Delta\Omega Ar_{ant}$ from ΔC_{ant} and the explicit buffer factors β_{DIC} and ω_{DIC}. Consequently, reductions smaller than 0.01 pH units (Figure 3) and 0.02 units (Figure 4), respectively, should be considered with caution.

Trends in any of the ancillary physical and biogeochemical variables that persist over time may affect the accuracy of the eMLR results (Levine et al., 2008) and it is difficult to estimate the total error in the eMLR in the presence of secular trends. For example, during the 1990s and 2000s the AAW was getting warmer and saltier (Ericson et al., 2014). Two warming events have been observed in the Nansen Basin (Korhonen et al., 2013). The first occurred in 1996 when the average temperature increased by 0.5°C in the lower Atlantic layer, extending into the Amundsen and Makarov Basins. Between 2001 and 2007, the second warming event exceeded the first event by 0.1°C but was limited to the Nansen Basin. This was also illustrated by Ericson et al. (2014) who looked at the depth integrated mean values of potential temperature and salinity for each water mass in the Nansen and Amundsen Basins over the period 1991–2011. They found limited decadal variability in the both temperature and salinity of all water masses but the AAW in the Nansen Basin. Adding a secular warming trend of 0.1°C and 0.5°C to the AAW data of the more recent data sets (2005–2015) in the Monte Carlo analysis above, the mean total uncertainty increased by 0.6 and 3 μmol/kg, respectively. In this study, we assume any secular trends in the ancillary physical and biogeochemical variables to be negligible and less than the total uncertainty of the eMLR analysis. For example, Ericson et al. (2014) reported no conceivable decadal trends in TA, PO_4, and NO_3 in the intermediate layers of the Eurasian Basin relative to the deep water (>2,000 m) over the period 1991–2011. The only significant trends found were those of increasing DIC (section 5.1) and, possibly, increasing deep water AOU (+0.4 $\mu mol \cdot kg^{-1} \cdot year^{-1}$).

Every technique used to determine temporal anthropogenic changes in DIC between two cruises is sensitive to biases in the data of either cruise. Such biases are not uncommon. Although values of DIC and TA are more

accurate after the introduction of CRMs, quality can vary between data sets (Bockmon & Dickson, 2015). In addition, the measurements of dissolved nutrients and oxygen occasionally remain inaccurate by several percent. Until primary measurements of required master parameters and ancillary parameters reach a level of sufficient accuracy, the interpretation of results of the back calculations and MLR-type methodology will be ambiguous to some extent, as is the choice of optimal predictors (Plancherel et al., 2013). This is important to consider when selecting the independent variables and when interpreting the results. Although a statistical fit of the natural variability of DIC can be within the uncertainty when using a different subset of predictors, it can result in unexpected and unrealistic features (section 3.1; Friis et al., 2005; Woosley et al., 2016).

Acknowledgments
Information about all of the data used in this analysis and how they can be accessed online is provided in Table 1 or referred to in the text. This work was supported by grants from the Swedish Research Council Formas (contract 214-2014-1165), the Royal Swedish Academy of Sciences, the YMER-80 Foundation, and logistic support from the Swedish Polar Research Secretariat. M. Karcher was partly funded by the TRIMODAL project (Arctic Ocean Flagship Project) of the FRAM Centre, Tromsø, Norway. N. Casacuberta acknowledges support from the Swiss National Science Foundation (AMBIZIONE PZ00P2_154805). This work is part of postdoctoral research (E. M. Jones) at the University of Groningen under the GEOTRACES program (H. J. W. de Baar). We thank Y. Luo and B. Boudreau for making their box model (Arctic.f) available. We thank P. Laan for technical and logistical support and S. Jutterström for pre-TransArc metadata discussions. Lastly, we would like to thank the two reviewers for their constructive critique that helped improve the manuscript.

References

Aksenov, Y., Bacon, S., Coward, A. C., & Nurser, A. J. G. (2010). The North Atlantic inflow to the Arctic Ocean: High-resolution model study. *Journal of Marine Systems*, *79*(1–2), 1–22. https://doi.org/10.1016/j.jmarsys.2009.05.003

Aldahan, A., Alfimov, V., & Possnert, G. (2007). ^{129}I anthropogenic budget: Major sources and sinks. *Applied Geochemistry*, *22*(3), 606–618. https://doi.org/10.1016/j.apgeochem.2006.12.006

Anderson, L. G., & Augstein, E. (1996). Polarstern 06AQ19960712 (AQN12) cruise data from the 1996 cruises. Oak Ridge, TN: Carbon Dioxide Information Analysis Center, Oak Ridge National Laboratory, US Department of Energy. https://doi.org/10.3334/CDIAC/otg.CARINA_06AQ19960712

Anderson, L. G., Ek, J., Ericson, Y., Humborg, C., Semiletov, I., Sundbom, M., & Ulfsbo, A. (2017). Export of calcium carbonate corrosive waters from the East Siberian Sea. *Biogeosciences*, *14*(7), 1811–1823. https://doi.org/10.5194/bg-14-1811-2017

Anderson, L. G., Jones, E. P., & Rudels, B. (1999). Ventilation of the Arctic Ocean estimated by a plume entrainment model constrained by CFCs. *Journal of Geophysical Research*, *104*(C6), 13,423–13,429. https://doi.org/10.1029/1999JC900074

Anderson, L. G., Tanhua, T., Jones, E. P., & Karlqvist, A. (2011). Hydrographic, chemical and carbon dioxide data from R/V Oden cruise 77DN20050819, August 19–September 25, 2005. Oak Ridge, TN: Carbon Dioxide Information Analysis Center, Oak Ridge National Laboratory, US Department of Energy. https://doi.org/10.3334/CDIAC/otg.CLIVAR_77DN20050819

Anderson, L. G., Ulfsbo, A., & Ericson, Y. (2011). Seawater carbonate chemistry in the Arctic Ocean during the F/S Polarstern cruise ARK-XXVI/3 in August–October, 2011. http://doi.pangaea.de/10.1594/PANGAEA.775817

Bates, N., Cai, W.-J., & Mathis, J. (2011). The ocean carbon cycle in the western Arctic Ocean: Distributions and air-sea fluxes of carbon dioxide. *Oceanography*, *24*(3), 186–201. https://doi.org/10.5670/oceanog.2011.71

Bates, N. R., Astor, Y. M., Church, M. J., Currie, K., Dore, J. E., Gonzáles-Dávila, M., et al. (2014). A time-series view of changing ocean chemistry due to ocean uptake of anthropogenic CO_2 and ocean acidification. *Oceanography*, *27*, 126–141. https://doi.org/10.5670/oceanog.2014.16

Bockmon, E. E., & Dickson, A. G. (2015). An inter-laboratory comparison assessing the quality of seawater carbon dioxide measurements. *Marine Chemistry*, *171*, 36–43. https://doi.org/10.1016/j.marchem.2015.02.002

Boudreau, B. P., Middelburg, J. J., Hofmann, A. F., & Meysman, F. J. R. (2010). Ongoing transients in carbonate compensation. *Global Biogeochemical Cycles*, *24*, GB4010. https://doi.org/10.1029/2009GB003654

Boudreau, B. P., Middelburg, J. J., & Meysman, F. J. R. (2010). Carbonate compensation dynamics. *Geophysical Research Letters*, *37*, L03603. https://doi.org/10.1029/2009GL041847

Brewer, P. G. (1978). Direct observation of the oceanic CO_2 increase. *Geophysical Research Letters*, *5*(12), 997–1000. https://doi.org/10.1029/GL005i012p00997

Brown, P. J., Bakker, D. C. E., Schuster, U., & Watson, A. J. (2010). Anthropogenic carbon accumulation in the subtropical North Atlantic. *Journal of Geophysical Research*, *115*, C04016. https://doi.org/10.1029/2008JC005043

Carter, B. R., Feely, R. A., Mecking, S., Cross, J. N., Macdonald, A. M., Siedlecki, S. A., et al. (2017). Two decades of Pacific anthropogenic carbon storage and ocean acidification along Global Ocean Ship-based Hydrographic Investigations Program sections P16 and P02. *Global Biogeochemical Cycles*, *31*, 306–327. https://doi.org/10.1002/2016GB005485

Casacuberta, N., Christl, M., Vockenhuber, C., Wefing, A.-M., Wacker, L., Masqué, P., et al. (2018). Tracing the three Atlantic branches entering the Arctic Ocean with 129I and 236U. *Journal of Geophysical Research: Oceans*, *123*. https://doi.org/10.1029/2018JC014168

Casacuberta, N., Masqué, P., Henderson, G., Rutgers van der Loeff, M., Bauch, D., Vockenhuber, C., et al. (2016). First ^{236}U data from the Arctic Ocean and use of ^{236}U/^{238}U and ^{129}I/^{236}U as a new dual tracer. *Earth and Planetary Science Letters*, *440*, 127–134. https://doi.org/10.1016/j.epsl.2016.02.020

Chen, G.-T., & Millero, F. J. (1979). Gradual increase of oceanic CO_2. *Nature*, *277*(5693), 205–206. https://doi.org/10.1038/277205a0

Chierici, M., & Fransson, A. (2009). Calcium carbonate saturation in the surface water of the Arctic Ocean: Undersaturation in freshwater influenced shelves. *Biogeosciences*, *6*(11), 2421–2431. https://doi.org/10.5194/bg-6-2421-2009

Chu, S. N., Wang, Z. A., Doney, S. C., Lawson, G. L., & Hoering, K. A. (2016). Changes in anthropogenic carbon storage in the Northeast Pacific in the last decade. *Journal of Geophysical Research: Oceans*, *121*, 4618–4632. https://doi.org/10.1002/2016JC011775

Clayton, T. D., & Byrne, R. H. (1993). Spectrophotometric seawater pH measurements: Total hydrogen ion concentration scale calibration of m-cresol purple and at-sea results. *Deep Sea Research (Part I, Oceanographic Research Papers)*, *40*(10), 2115–2129. https://doi.org/10.1016/0967-0637(93)90048-8

Conway, T. J., Tans, P. P., Waterman, L. S., Thoning, K. W., Kitzis, D. R., Masarie, K. A., & Zhang, N. (1994). Evidence for interannual variability of the carbon cycle from the National Oceanic and Atmospheric Administration/Climate Monitoring and Diagnostics Laboratory Global Air Sampling Network. *Journal of Geophysical Research*, *99*(D11), 22,831–22,855. https://doi.org/10.1029/94JD01951

Dickson, A. G. (1990). Standard potential of the reaction: AgCl(s) + 1/2H2(g) = Ag(s) + HCl(aq), and the standard acidity constant of the ion HSO_4^- in synthetic sea water from 273.15 to 318.15 K. *Journal of Chemical Thermodynamics*, *22*(2), 113–127. https://doi.org/10.1016/0021-9614(90)90074-Z

Egleston, E. S., Sabine, C. L., & Morel, F. M. M. (2010). Revelle revisited: Buffer factors that quantify the response of ocean chemistry to changes in DIC and alkalinity. *Global Biogeochemical Cycles*, *24*, GB1002. https://doi.org/10.1029/2008GB003407

Ericson, Y., Ulfsbo, A., van Heuven, S., Kattner, G., & Anderson, L. G. (2014). Increasing carbon inventory of the intermediate layers of the Arctic Ocean. *Journal of Geophysical Research: Oceans*, *119*, 2312–2326. https://doi.org/10.1002/2013JC009514

Fransson, A., Chierici, M., Miller, L. A., Carnat, G., Shadwick, E., Thomas, H., et al. (2013). Impact of sea-ice processes on the carbonate system and ocean acidification at the ice-water interface of the Amundsen Gulf, Arctic Ocean. *Journal of Geophysical Research: Oceans*, *118*, 7001–7023. https://doi.org/10.1002/2013JC009164

Friis, K., Körtzinger, A., Pätsch, J., & Wallace, D. W. R. (2005). On the temporal increase of anthropogenic CO_2 in the subpolar North Atlantic. *Deep Sea Research Part I: Oceanographic Research Papers*, *52*(5), 681–698. https://doi.org/10.1016/j.dsr.2004.11.017

Gammon, R. H., Cline, J., & Wisegarver, D. (1982). Chlorofluoromethanes in the northeast Pacific Ocean: Measured vertical distributions and application as transient tracers of upper ocean mixing. *Journal of Geophysical Research*, *87*(C12), 9441–9454. https://doi.org/10.1029/JC087iC12p09441

Gascard, J.-C., Raisbeck, G., Sequeira, S., Yiou, F., & Mork, K. A. (2004). The Norwegian Atlantic Current in the Lofoten basin inferred from hydrological and tracer data (^{129}I) and its interaction with the Norwegian Coastal Current. *Geophysical Research Letters*, *31*, L01308. https://doi.org/10.1029/2003GL018303

Gordon, L. I., Jennings, J. C., Ross, A. A., & Krest, J. M. (1994). A suggested protocol for continuous flow automated analysis of seawater nutrients (phosphate, nitrate, nitrite and silicic acid) in the WOCE Hydrographic Program and the Joint Global Ocean Fluxes Study (*Report*). MA, USA: WOCE Operations Manual, WHP Off. Rep. WHPO 91-1, WOCE Rep. 68/91, rev. 1 Woods Hole.

Gruber, N., Sarmiento, J. L., & Stocker, T. F. (1996). An improved method for detecting anthropogenic CO_2 in the oceans. *Global Biogeochemical Cycles*, *10*(4), 809–837. https://doi.org/10.1029/96GB01608

Hagens, M., & Middelburg, J. J. (2016). Generalised expressions for the response of pH to changes in ocean chemistry. *Geochimica et Cosmochimica Acta*, *187*, 334–349. https://doi.org/10.1016/j.gca.2016.04.012

Hall, T. M., Haine, T. W. N., & Waugh, D. W. (2002). Inferring the concentration of anthropogenic carbon in the ocean from tracers. *Global Biogeochemical Cycles*, *16*(4), 1131. https://doi.org/10.1029/2001GB001835

Haraldsson, C., Anderson, L. G., Hassellöv, M., Hulth, S., & Olsson, K. (1997). Rapid, high-precision potentiometric titration of alkalinity in ocean and sediment pore waters. *Deep Sea Research Part I*, *44*(12), 2031–2044. https://doi.org/10.1016/S0967-0637(97)00088-5

Hauck, J., & Völker, C. (2015). Rising atmospheric CO_2 leads to large impact of biology on Southern Ocean CO_2 uptake via changes of the Revelle factor. *Geophysical Research Letters*, *42*, 1459–1464. https://doi.org/10.1002/2015GL063070

Hauck, J., Hoppema, M., Bellerby, R. G. J., Völker, C., & Wolf-Gladrow, D. (2010). Data-based estimation of anthropogenic carbon and acidification in the Weddell Sea on a decadal timescale. *Journal of Geophysical Research*, *115*, C03004. https://doi.org/10.1029/2009JC005479

He, P., Hou, X., Aldahan, A., Possnert, G., & Yi, P. (2013). Iodine isotopes species fingerprinting environmental conditions in surface water along the northeastern Atlantic Ocean. *Scientific Reports*, *3*, 2685. https://doi.org/10.1038/srep02685

Johnson, K. M., Sieburth, J. M., Williams, P. J. l., & Brändström, L. (1987). Coulometric total carbon dioxide analysis for marine studies: Automation and calibration. *Marine Chemistry*, *21*(2), 117–133. https://doi.org/10.1016/0304-4203(87)90033-8

Jones, E. M., & Ulfsbo, A. (2017). Seawater carbonate chemistry measured on water bottle samples during POLARSTERN cruise PS94 (ARK-XXIX/3). http://doi.pangaea.de/10.1594/PANGAEA.XXXXXX

Jutterström, S., & Anderson, L. G. (2005). The saturation of calcite and aragonite in the Arctic Ocean. *Marine Chemistry*, *94*(1–4), 101–110. https://doi.org/10.1016/j.marchem.2004.08.010

Jutterström, S., Anderson, L. G., Bates, N. R., Bellerby, R., Johannessen, T., Jones, E. P., et al. (2010). Arctic Ocean data in CARINA. *Earth System Science Data*, *2*(1), 71–78. https://doi.org/10.5194/essd-2-71-2010

Karcher, M., Smith, J. N., Kauker, F., Gerdes, R., & Smethie, W. M. (2012). Recent changes in Arctic Ocean circulation revealed by iodine-129 observations and modeling. *Journal of Geophysical Research*, *117*, C08007. https://doi.org/10.1029/2011JC007513

Kattner, G., & Ludwichowski, K.-U. (2014). Inorganic nutrients measured on water bottle samples during POLARSTERN cruise ARK-XXVI/3 (TransArc). https://doi.pangaea.de/10.1594/PANGAEA.832164

Kershaw, P., & Baxter, A. (1995). The transfer of reprocessing wastes from north-west Europe to the Arctic. *Deep Sea Research Part II: Topical Studies in Oceanography*, *42*(6), 1413–1448. https://doi.org/10.1016/0967-0645(95) 00048-8

Key, R. M., Olsen, A., van Heuven, S., Lauvset, S. K., Velo, A., Lin, X., et al. (2015). Global Ocean Data Analysis Project, Version 2 (GLODAPv2), ORNL/CDIAC-162, ND-P093. Oak Ridge, TN: Carbon Dioxide Information Analysis Center, Oak Ridge National Laboratory, US Department of Energy. https://doi.org/10.3334/CDIAC/OTG.NDP093_GLODAPv2

Key, R. M., Tanhua, T., Olsen, A., Hoppema, M., Jutterström, S., Schirnick, C., et al. (2010). The CARINA data synthesis project: Introduction and overview. *Earth System Science Data*, *2*(1), 105–121. https://doi.org/10.5194/essd-2-105-2010

Khatiwala, S., Tanhua, T., Mikaloff Fletcher, S., Gerber, M., Doney, S. C., Graven, H. D., et al. (2013). Global ocean storage of anthropogenic carbon. *Biogeosciences*, *10*(4), 2169–2191. https://doi.org/10.5194/bg-10-2169-2013

Korhonen, M., Rudels, B., Marnela, M., Wisotzki, A., & Zhao, J. (2013). Time and space variability of freshwater content, heat content and seasonal ice melt in the Arctic Ocean from 1991 to 2011. *Ocean Science*, *9*(6), 1015–1055. https://doi.org/10.5194/os-9-1015-2013

Lavigne, H., & Gattuso, J. P. (2010). seacarb: Seawater carbonate chemistry with R.version 3.1.1. Retrieved from https://cran.R-project.org/package=seacarb

Le Quéré, C., Andrew, R. M., Canadell, J. G., Sitch, S., Korsbakken, J. I., Peters, G. P., et al. (2016). Global carbon budget 2016. *Earth System Science Data*, *8*(2), 605–649. https://doi.org/10.5194/essd-8-605-2016

Levine, N. M., Doney, S. C., Wanninkhof, R., Lindsay, K., & Fung, I. Y. (2008). Impact of ocean carbon system variability on the detection of temporal increases in anthropogenic CO_2. *Journal of Geophysical Research*, *113*, C03019. https://doi.org/10.1029/2007JC004153

Liu, X., Patsavas, M. C., & Byrne, R. H. (2011). Purification and characterization of meta-cresol purple for spectrophotometric seawater pH measurements. *Environmental Science & Technology*, *45*(11), 4862–4868. https://doi.org/10.1021/es200665d

Lueker, T. J., Dickson, A. G., & Keeling, C. D. (2000). Ocean pCO_2 calculated from dissolved inorganic carbon, alkalinity, and equations for K_1 and K_2: Validation based on laboratory measurements of CO_2 in gas and seawater at equilibrium. *Marine Chemistry*, *70*(1-3), 105–119. https://doi.org/10.1016/S0304-4203(00)00022-0

Luo, Y., Boudreau, B. P., & Mucci, A. (2016). Disparate acidification and calcium carbonate desaturation of deep and shallow waters of the Arctic Ocean. *Nature Communications*, *7*(12), 821. https://doi.org/10.1038/ncomms12821

Mauritzen, C. (1996). Production of dense overflow waters feeding the North Atlantic across the Greenland-Scotland Ridge. Part 1: Evidence for a revised circulation scheme. *Deep Sea Research (Part I Oceanographic Research Papers)*, *43*(6), 769–806. https://doi.org/10.1016/0967-0637(96)00037-4

Olsen, A., Key, R. M., van Heuven, S., Lauvset, S. K., Velo, A., Lin, X., et al. (2016). An internally consistent data product for the world ocean: The Global Ocean Data Analysis Project, version 2 (GLODAPv2). *Earth System Science Data Discussion*, *2016*, 1–78. https://doi.org/10.5194/essd-2015-42

Olsen, A., Omar, A. M., Bellerby, R. G. J., Johannessen, T., Ninnemann, U., Brown, K. R., et al. (2006). Magnitude and origin of the anthropogenic CO_2 increase and ^{13}C Suess effect in the Nordic seas since 1981. *Global Biogeochemical Cycles*, *20*, GB3027. https://doi.org/10.1029/2005GB002669

Omar, A., Johannessen, T., Kaltin, S., & Olsen, A. (2003). Anthropogenic increase of oceanic pCO_2 in the Barents Sea surface water. *Journal of Geophysical Research*, *108*(C12), 3388. https://doi.org/10.1029/2002JC001628

Peng, T.-H., & Wanninkhof, R. (2010). Increase in anthropogenic CO_2 in the Atlantic Ocean in the last two decades. *Deep Sea Research Part I: Oceanographic Research Papers*, *57*(6), 755–7700. https://doi.org/10.1016/j.dsr.2010.03.008

Peng, T.-H., Wanninkhof, R., Bullister, J. L., Feely, R. A., & Takahashi, T. (1998). Quantification of decadal anthropogenic CO_2 uptake in the ocean based on dissolved inorganic carbon measurements. *Nature*, *396*(6711), 560–563.

Plancherel, Y., Rodgers, K. B., Key, R. M., Jacobson, A. R., & Sarmiento, J. L. (2013). Role of regression model selection and station distribution on the estimation of oceanic anthropogenic carbon change by eMLR. *Biogeosciences*, *10*(7), 4801–4831. https://doi.org/10.5194/bg-10-4801-2013

Pnyushkov, A. V., Polyakov, I. V., Ivanov, V. V., Aksenov, Y., Coward, A. C., Janout, M., & Rabe, B. (2015). Structure and variability of the boundary current in the Eurasian Basin of the Arctic Ocean. *Deep Sea Research Part I: Oceanographic Research Papers*, *101*, 80–97. https://doi.org/10.1016/j.dsr.2015.03.001

Polyakov, I. V., Pnyushkov, A. V., Alkire, M. B., Ashik, I. M., Baumann, T. M., Carmack, E. C., et al. (2017). Greater role for Atlantic inflows on sea-ice loss in the Eurasian Basin of the Arctic Ocean. *Science*, *356*(6335), 285–291. https://doi.org/10.1126/science.aai8204

Postma, H. (1964). The exchange of oxygen and carbon dioxide between the ocean and the atmosphere. *Netherlands Journal of Sea Research*, *2*(2), 258–283. https://doi.org/10.1016/0077-7579(64)90013-4

Qi, D., Chen, L., Chen, B., Gao, Z., Zhong, W., Feely, R. A., et al. (2017). Increase in acidifying water in the western Arctic Ocean. *Nature Climate Change*, *7*, 195–199. https://doi.org/10.1038/nclimate3228

Quay, P., Sonnerup, R., Stutsman, J., Maurer, J., Körtzinger, A., Padin, X. A., & Robinson, C. (2007). Anthropogenic CO_2 accumulation rates in the North Atlantic Ocean from changes in the $^{13}C/^{12}C$ of dissolved inorganic carbon. *Global Biogeochemical Cycles*, *21*, GB1009. https://doi.org/10.1029/2006GB002761

Rabe, B., Schauer, U., Ober, S., Horn, M., Hoppmann, M., Korhonen, M., et al. (2016). Physical oceanography measured on water bottle samples during POLARSTERN cruise PS94 (ARK-XXIX/3). http://doi.pangaea.de/10.1594/PANGAEA.859559

Revelle, R. (1983). The oceans and the carbon-dioxide problem. *Oceanus*, *26*(2), 3–9.

Rudels, B. (2016). Arctic Ocean stability: The effects of local cooling, oceanic heat transport, freshwater input, and sea ice melt with special emphasis on the Nansen Basin. *Journal of Geophysical Research: Oceans*, *121*, 4450–4473. https://doi.org/10.1002/2015JC011045

Rudels, B., Anderson, L., Eriksson, P., Fahrbach, E., Jakobsson, M., & Jones, E. P. (2012). Observations in the ocean. In H.-W. Jacobi (Ed.), *Arctic climate change, Atmospheric and Oceanographic Sciences Library, book section 4* (Vol. 43, pp. 117–198). Dordrecht: Springer. https://doi.org/10.1007/978-94-007-2027-5_4

Sabine, C. L., Feely, R. A., Gruber, N., Key, R. M., Lee, K., Bullister, J. L., et al. (2004). The oceanic sink for anthropogenic CO_2. *Science*, *305*(5682), 367–371. https://doi.org/10.1126/science.1097403

Sabine, C. L., Feely, R. A., Millero, F. J., Dickson, A. G., Langdon, C., Mecking, S., & Greeley, D. (2008). Decadal changes in Pacific carbon. *Journal of Geophysical Research*, *113*, C07021. https://doi.org/10.1029/2007JC004577

Schauer, U., Rabe, B., & Wisotzki, A. (2011). Physical oceanography during POLARSTERN cruise ARK-XXVI/3. http://doi.pangaea.de/10.1594/PANGAEA.774181

Semiletov, I., Pipko, I., Gustafsson, O., Anderson, L. G., Sergienko, V., et al. (2016). Acidification of East Siberian Arctic Shelf waters through addition of freshwater and terrestrial carbon. *Nature Geoscience*, *9*(5), 361–365. https://doi.org/10.1038/ngeo2695

Serreze, M. C., & Barry, R. G. (2011). Processes and impacts of Arctic amplification: A research synthesis. *Global and Planetary Change*, *77*(1), 85–96. https://doi.org/10.1016/j.gloplacha.2011.03.004

Skjelvan, I., Falck, E., Rey, F., & Kringstad, S. B. (2008). Inorganic carbon time series at Ocean Weather Station M in the Norwegian Sea. *Biogeosciences*, *5*(2), 549–560. https://doi.org/10.5194/bg-5-549-2008

Smith, J. N., McLaughlin, F. A., Smethie, W. M., Moran, S. B., & Lepore, K. (2011). Iodine-129, ^{137}Cs, and CFC-11 tracer transit time distributions in the Arctic Ocean. *Journal of Geophysical Research*, *116*, C04024. https://doi.org/10.1029/2010JC006471

Steinacher, M., Joos, F., Frölicher, T. L., Plattner, G. K., & Doney, S. C. (2009). Imminent ocean acidification in the Arctic projected with the NCAR global coupled carbon cycle-climate model. *Biogeosciences*, *6*(4), 515–533. https://doi.org/10.5194/bg-6-515-2009

Stöven, T., Tanhua, T., Hoppema, M., & von Appen, W. J. (2016). Transient tracer distributions in the Fram Strait in 2012 and inferred anthropogenic carbon content and transport. *Ocean Science*, *12*(1), 319–333. https://doi.org/10.5194/os-12-319-2016

Tanhua, T., Bates, N., & Körtzinger, A. (2013). The marine carbon cycle and ocean carbon inventories report. In C. J. (Ed.), *Ocean Circulation and Climate: A 21st Century Perspective. International Geophysics* (2nd ed., Vol. 103, pp. 787–815). Oxford: Academic Press. https://doi.org/10.1016/B978-0-12-391851-2. 00030-1

Tanhua, T., Jones, E. P., Jeansson, E., Jutterström, S., Smethie, W. M., Wallace, D. W. R., & Anderson, L. G. (2009). Ventilation of the Arctic Ocean: Mean ages and inventories of anthropogenic CO_2 and CFC-11. *Journal of Geophysical Research*, *114*, C01002. https://doi.org/10.1029/2008JC004868

Tanhua, T., Körtzinger, A., Friis, K., Waugh, D. W., & Wallace, D. W. R. (2007). An estimate of anthropogenic CO_2 inventory from decadal changes in oceanic carbon content. *Proceedings of the National Academy of Sciences*, *104*(9), 3037–3042. https://doi.org/10.1073/pnas.0606574104

Uppström, L. R. (1974). The boron/chlorinity ratio of deep-sea water from the Pacific Ocean. *Deep Sea Research and Oceanographic Abstracts*, *21*(2), 161–162. https://doi.org/10.1016/0011-7471(74)90074-6

van Heuven, S., Pierrot, D., Lewis, E., & Wallace, D. W. R. (2011). MATLAB program developed for CO_2 system calculations, ORNL/CDIAC-105b. Oak Ridge, TN: Carbon Dioxide Information Analysis Center, Oak Ridge National Laboratory, U.S. Department of Energy.

van Heuven, S. M. A. C., Hoppema, M., Huhn, O., Slagter, H. A., & de Baar, H. J. W. (2011). Direct observation of increasing CO_2 in the Weddell Gyre along the Prime Meridian during 1973–2008. *Deep Sea Research Part II: Topical Studies in Oceanography*, *58*(25–26), 2613–2635. https://doi.org/10.1016/j.dsr2.2011.08.007

van Ooijen, J. C., Rijkenberg, M. J. A., Gerringa, L. J. A., Rabe, B., & Rutgers van der Loeff, M. M. (2016). Inorganic nutrients measured on water bottle samples during POLARSTERN cruise PS94. https://doi.pangaea.de/10.1594/PANGAEA.868396

Velo, A., Pérez, F. F., Lin, X., Key, R. M., Tanhua, T., de la Paz, M., et al. (2010). CARINA data synthesis project: pH data scale unification and cruise adjustments. *Earth System Science Data*, *2*(1), 133–155. https://doi.org/10.5194/essd-2-133-2010

Wallace, D. W. R. (1995). Monitoring global ocean carbon inventories (Report, OOSDP Background Report, No. 5). TX: Texas AUniversity College Stations.

Wanninkhof, R., Doney, S. C., Bullister, J. L., Levine, N. M., Warner, M., & Gruber, N. (2010). Detecting anthropogenic CO_2 changes in the interior Atlantic Ocean between 1989 and 2005. *Journal of Geophysical Research*, *115*, C11028. https://doi.org/10.1029/2010JC006251

Waters, J. F., Millero, F. J., & Sabine, C. L. (2011). Changes in South Pacific anthropogenic carbon. *Global Biogeochemical Cycles*, *25*, GB4011. https://doi.org/10.1029/2010GB003988

Williams, N. L., Feely, R. A., Sabine, C. L., Dickson, A. G., Swift, J. H., Talley, L. D., & Russell, J. L. (2015). Quantifying anthropogenic carbon inventory changes in the Pacific sector of the Southern Ocean. *Marine Chemistry*, *174*(Supplement C), 147–160. https://doi.org/10.1016/j.marchem.2015.06.015

Woosley, R. J., Millero, F. J., & Wanninkhof, R. (2016). Rapid anthropogenic changes in CO_2 and pH in the Atlantic Ocean: 2003–2014. *Global Biogeochemical Cycles*, *30*, 70–90. https://doi.org/10.1002/2015GB005248

Woosley, R. J., Millero, F. J., & Takahashi, T. (2017). Internal consistency of the inorganic carbon system in the Arctic Ocean. *Limnology and Oceanography: Methods*, *15*(10), 887–896. https://doi.org/10.1002/lom3.10208

Wynn, J. G., Robbins, L. L., & Anderson, L. G. (2016). Processes of multibathyal aragonite undersaturation in the Arctic Ocean. *Journal of Geophysical Research: Oceans*, *121*, 1–21. https://doi.org/10.1002/2016JC011696

Yamamoto, A., Kawamiya, M., Ishida, A., Yamanaka, Y., & Watanabe, S. (2012). Impact of rapid sea-ice reduction in the Arctic Ocean on the rate of ocean acidification. *Biogeosciences*, *9*(6), 2365–2375. https://doi.org/10.5194/bg-9-2365-2012

Yamamoto-Kawai, M., McLaughlin, F. A., Carmack, E. C., Nishino, S., & Shimada, K. (2009). Aragonite undersaturation in the Arctic Ocean: Effects of ocean acidification and sea ice melt. *Science*, *326*(5956), 1098–1100. https://doi.org/10.1126/science.1174190